Received: Added at production | Revised: Added at production | Accepted: Added at production

DOI: xxx/xxxx

ARTICLE TYPE

Reduced order mathematical homogenization method for polycrystalline microstructure with microstructurally small cracks

Damin Xia[1] | Caglar Oskay[1]*

[1]Department of Civil and Environmental Engineering, Vanderbilt University, Nashville, TN, United States of America

Correspondence
*Caglar Oskay.
Email: caglar.oskay@vanderbilt.edu

Present Address
VU Station B#351831, 2301 Vanderbilt Place, Nashville, TN 37235, United States of America

Abstract

In this manuscript, a reduced order homogenization model is developed for polycrystalline microstructures with microstructurally small cracks. The proposed approach employs and advances the eigendeformation-based homogenization method to account for the plastic deformation within the microstructure and the presence of cracks. A novel approach to construct the reduced order basis for the separation field is proposed for approximating crack opening profiles of kinked cracks. To capture the variable stress fields around the crack tips, a domain partitioning strategy that automatically refines the reduced order parts in these regions is proposed. The model performance is evaluated against reference crystal plasticity finite element (CPFE) simulations under various loading conditions and crack configurations. Both the overall and local response predictions show reasonable accuracy with only a fraction of the computational cost of the reference simulations.

KEYWORDS:
Microstructurally small cracks; Crystal plasticity; Computational homogenization; Reduced order modeling

1 | INTRODUCTION

Defects in material microstructures often serve as the nucleation sites for the observed failure in structural materials. A quintessential example of this is fatigue initiation in polycrystalline materials (e.g., metals and alloys), where formation and growth of microstructurally small cracks (MSCs) contribute to a significant portion of the overall life of the material, particularly in high cycle or very high cycle regimes.[1]. MSCs are cracks at the scale of the material microstructure, the growth of which is significantly affected by the local material characteristics (e.g., grain orientations, presence of subgrain features, grain boundaries, etc.).

From the computational material modeling perspective, an important issue is how to predict the effects of MSCs on the microstructural behavior in a computationally efficient fashion. Computational efficiency is a critical issue because microstructural analysis must either be tied to uncertainty quantification to account for the inherent randomness in the morphological features[2] and properties at the microstructural scale, or to multiscale analyses where the performance and failure at the macroscopic scale[3] is assessed. In either case, a large number of microstructural simulations are necessary.

The Crystal Plasticity Finite Element (CPFE) method [4,5] and spectral methods based on the Fast Fourier Transform (FFT)[6,7] are commonly used to evaluate the microstructural response of polycrystalline materials at small length scales that can still be considered as continuum. FFT offers significant computational efficiency compared with CPFE[8], but is somewhat restricted due to limitations on boundary conditions, the need to use uniform grid, and the presence of oscillations in the response due to

the Gibbs' phenomenon particularly in the presence of sharp material property changes in the microstructure[9,10]. In the context of CPFE, the presence and propagation of cracks in a microstructure have been modeled by combining CPFE with adaptive crack insertion approaches[11,12], extended finite element method (XFEM)[13,14], cohesive zone models (CZM)[15,16], or phase field models (PFM) of fracture[17,18,19]. More recently, Rovinelli et al.[10] examined the response fields near a crack tip using both FFT and CPFE methods coupled with crack insertion and showed that FFT predicts comparable response fields to CPFE. Direct insertion of cracks with complex morphologies into FFT presents additional difficulty due to the constraints imposed by the uniform grid. Ma and Sun[20] recently combined FFT with PFM, where cracks of complex morphologies can be represented in a polycrystalline microstructure. A primary disadvantage of the FFT and CPFE methods for short crack modeling is that they remain computationally expensive, particularly when the crack morphologies are complex.

Reduced order models (ROMs) offer a computationally efficient alternative to direct numerical simulation of the polycrystalline volumes using CPFE or FFT. Several approaches have been proposed in this regard that include visco-plastic self-consistent (VPSC) models[21,22], nonuniform transformation field analysis (NTFA)[23], proper orthogonal decomposition (POD)[24], self-consistent clustering method (SCA)[25,26], parametrically homogenized constitutive model (PHCM)[27], proper generalized decomposition[28], grain cluster method[29,30] and eigenstrain based computational homogenization method[31,32,33,34,35], among others. More recently, data-driven models based on machine learning are attracting significant attention[36,37,38,39,40,41] and particularly those that follow physical constraints offer a promising alternative pathway. To the best of the authors' knowledge, very few reduced order models account for the presence of cracks. In the context of inclusion and fiber reinforced composites, Oskay and Fish[42] proposed the eigendeformation-based homogenization approach (EHM) approach, which is a generalization of the eigenstrain-based homogenization to account for interfacial cracks. Brandyberry et al.[43] recently implemented a generalized FEM version of the formulation to study interface damage. Liu[44] proposed the use of a deep material network to represent progressive interface debonding in unidirectional fiber-reinforced composites. Oliver et al.[45] proposed hyper-reduction methodology that builds on the continuum strong discontinuity formulation and represents fracture in random composites. Oskay et al.[3] recently proposed the multiscale discrete damage theory for fiber reinforced composites, in which, a set of discrete cohesive potential failure surfaces are defined over surface morphologies and represented using a reduced approximation basis. This approach takes into account the formation and presence of "microstructurally long" cracks that run across the entire microstructure.

In this manuscript, a reduced order formulation is proposed for polycrystalline materials with microstructurally short cracks. The proposed formulation leverages the EHM framework[3,31], where the eigenstrain concept is used to account for the viscoplastic deformation within the volume, whereas the eigenseparation concept is used to account for the presence of cracks. This manuscript has the following novel contributions: (1) the EHM formulation is extended to account for cracks that begin and end within the material microstructure, hence the proposed reduced order model captures the stress and strain concentrations due to the presence of cracks; (2) a reduced basis construction algorithm for the phases has been developed to accurately account for the stress fields in the fracture process zone; (3) a reduced basis construction procedure for the crack separation field has been developed to describe crack opening under a wide range of load states. The proposed formulation has been implemented in the context of quasi-2D microstructures in the presence of multiple and kinked short cracks. The verification of the proposed ROM is conducted by comparing the efficiency and accuracy of the model with the CPFE simulations under various loading conditions and crack configurations.

The remainder of the manuscript is organized as follows: The overview of the ROM formulation is introduced in Section 2. The construction of the reduced basis for the crack separation fields is discussed in Section 3. Section 4 presents the partitioning algorithm to refine the reduced order parts for the viscoplastic phases around the crack tips. The numerical implementation of the proposed model is discussed in Section 5. Section 6 provides numerical verification. Conclusions and future works are discussed in Section 7.

2 | OVERVIEW OF EHM FORMULATION

The reduced order modeling formulation based on the EHM approach was previously proposed in Refs.[3,31,42]. In what follows, a brief overview of the formulation is presented to provide context for the construction of reduced order basis functions in the presence of short cracks.

Let $\Theta \subset \mathbb{R}^{n_{sd}}$ ($n_{sd} = 2, 3$) denote the domain of a polycrystalline volume at the scale of the material microstructure. The volume consists of n_{grain} grains ($\Theta_i \subset \Theta$ denotes the domain of i^{th} grain) and includes n_{cracks} short cracks. Domain of the i^{th}

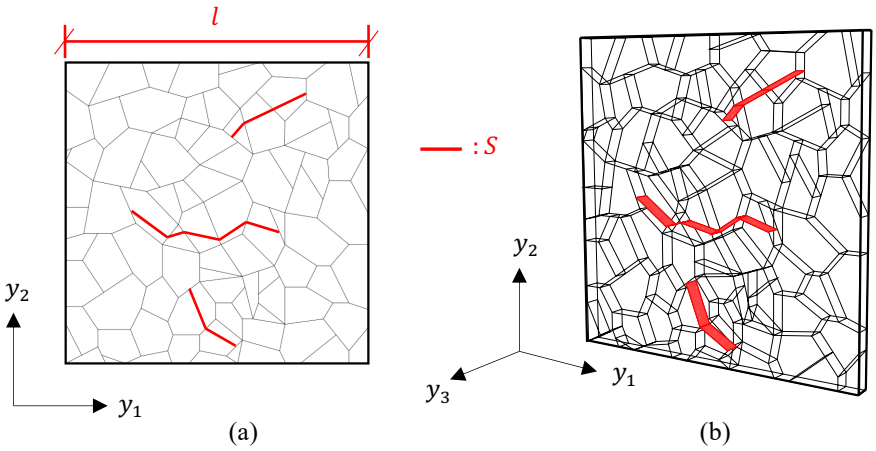

Figure 1 Two-dimensional microstructure with cracks: (a) 2D and (b) Quasi-2D

crack is denoted as $S_i := \left\{\mathbf{y}(s) | s \in J_i \subset \mathbb{R}^{n_{sd}-1}\right\}$. As notionally denoted in Fig. 1, we consider two-dimensional or quasi two-dimensional volumes, where the cracks extend through the out-of-plane direction (i.e., y_3). We focus only on transgranular cracks because the dominant mechanism of high cycle fatigue failure in unalloyed titanium and most α/β titanium alloys has been observed to be transgranular cracking of the α phase[46,47,48], although they do not distinguish from intergranular cracks from the perspective of the current framework. It is possible to consider a range of crack morphologies (e.g., kinked, curved, branching etc.) that may occur under different boundary and loading conditions. When subjected to static and cyclic loading, formation and growth of short cracks are heavily influenced by the underlying grain/subgrain structure that often results in kinked (i.e., piecewise straight) cracks[49,50,51]. Curved cracks can be approximated by piece-wise straight cracks i.e., a crack with many kinks. Branching cracks are more likely to occur under dynamic loading, which is out of the scope of the current study. We therefore focus our attention only on kinked crack configurations.

Under the action of applied loading, part of or the whole polycrystalline volume deforms inelastically. The governing equilibrium equation is expressed in the following form:

$$\left\{L_{ijkl}(\mathbf{y})\left[\epsilon_{kl}(\mathbf{y},t) - \mu_{kl}(\mathbf{y},t)\right]\right\}_{,y_j} = 0 \tag{1}$$

where, $\mathbf{L}$ is the tensor of elastic moduli, and $\boldsymbol{\epsilon}$ and $\boldsymbol{\mu}$ respectively denote the total and inelastic strain fields. The domain is subjected to a macroscopic strain history (i.e., $\bar{\boldsymbol{\epsilon}}(t)$) which serves as the forcing function. The following unilateral contact conditions are imposed along the crack facets ($\mathbf{y} \in S; S := \bigcup_{i=1}^{n_{\text{cracks}}} S_i$):

$$\delta_N(\mathbf{y},t) \geq 0; \quad t_N(\mathbf{y},t) \leq 0; \quad t_N(\mathbf{y},t)\delta_N(\mathbf{y},t) = 0 \tag{2}$$

where t_N and δ_N are normal components of traction and displacement jump (or separation) along the crack paths, respectively. The evolution of inelastic strain due to crystallographic slip along preferred slip orientations within a grain is expressed as:

$$\dot{\mu}_{ij}(\mathbf{y},t) = \sum_{s=1}^{N} \dot{\gamma}^s(\mathbf{y},t) Z^s_{ij}(\mathbf{y}) \tag{3}$$

where, $\dot{\gamma}^s$ is the plastic shearing rate on the s^{th} slip system, the evolution of which is described by a crystal plasticity model, N is the total number of slip systems, and $\mathbf{Z}^s$ is the Schmid tensor.

We proceed with the following ansatz for the strain field following[3,31,42]:

$$\epsilon_{ij}(\mathbf{y},t) = A_{ijkl}(\mathbf{y})\bar{\epsilon}_{kl}(t) + \int_{\Theta} g^{\text{ph}}_{ijkl}(\mathbf{y},\hat{\mathbf{y}})\mu_{kl}(\hat{\mathbf{y}},t)d\hat{\mathbf{y}} + \int_{S} g^{\text{sep}}_{ijk}(\mathbf{y},\hat{\mathbf{y}})\delta_k(\hat{\mathbf{y}},t)d\hat{\mathbf{y}} \tag{4}$$

where $\mathbf{A} = \mathbf{G} + \mathbf{I}$ and $\mathbf{I}$ is the fourth order identity tensor, $\mathbf{G}$, $\mathbf{g}^{\text{ph}}$ and $\mathbf{g}^{\text{sep}}$ are the polarization functions that are the symmetric gradients of the influence functions (i.e., $\mathbf{G} = \nabla^{\text{sym}}\mathbf{H}$, $\mathbf{g}^{\text{ph}} = \nabla^{\text{sym}}\mathbf{h}^{\text{ph}}$ and $\mathbf{g}^{\text{sep}} = \nabla^{\text{sym}}\mathbf{h}^{\text{sep}}$), $\mathbf{H}$ is the elastic influence function, $\mathbf{h}^{\text{ph}}$ is the inelastic (or phase) influence function, and $\mathbf{h}^{\text{sep}}$ is the separation influence function that accounts for the existence of cracks within the microstructure. $\boldsymbol{\delta}$ is the displacement jump (or separation) along the crack facets. The boundary conditions are

chosen to ensure:

$$\left\langle \epsilon_{ij}(\mathbf{y},t)\right\rangle_{\Theta} = \bar{\epsilon}_{ij}(t) \tag{5}$$

where $\langle\rangle_{\Theta}$ means volume average over domain Θ and $\bar{\epsilon}$ is the macroscopic strain. This condition could be satisfied by using periodic, homogeneous displacement, homogeneous traction boundary conditions, or combinations of them[52].

Substituting Eq. (4) into Eq. (1) yields an alternative form of the equilibrium equation:

$$\left\{ L_{ijkl}(\mathbf{y}) \left[A_{klmn}(\mathbf{y})\bar{\epsilon}_{mn}(t) + \int_{\Theta} [g^{\text{ph}}_{klmn}(\mathbf{y},\hat{\mathbf{y}}) - I_{klmn}\delta(\mathbf{y}-\hat{\mathbf{y}})] \;\; \mu_{mn}(\hat{\mathbf{y}},t)d\hat{\mathbf{y}} + \int_{S} g^{\text{sep}}_{klm}(\mathbf{y},\hat{\mathbf{y}})\delta_m(\hat{\mathbf{y}},t)d\hat{\mathbf{y}} \right] \right\}_{,y_j} = 0 \tag{6}$$

where δ is the Dirac delta distribution. Pre-multiplying Eq. (6) with the separation influence function $\mathbf{h}^{\text{sep}}$, integrating by parts over the microstructure domain, and utilizing periodicity yield:

$$\begin{aligned} t_p(\hat{\mathbf{y}},t) + \int_{\Theta} g^{\text{sep}}_{ijp}(\mathbf{y},\hat{\mathbf{y}}) L_{ijkl}(\mathbf{y}) \Bigg[& A_{klmn}(\mathbf{y})\bar{\epsilon}_{mn}(t) + \\ & \int_{\Theta} [g^{\text{ph}}_{klmn}(\mathbf{y},\tilde{\mathbf{y}}) - I_{klmn}\delta(\mathbf{y}-\tilde{\mathbf{y}})]\mu_{mn}(\tilde{\mathbf{y}},t)d\tilde{\mathbf{y}} + \int_{S} g^{\text{sep}}_{klm}(\mathbf{y},\tilde{\mathbf{y}})\delta_m(\tilde{\mathbf{y}},t)d\tilde{\mathbf{y}} \Bigg] d\mathbf{y} = 0 \end{aligned} \tag{7}$$

where $\mathbf{t}$ is the traction along the crack facets. Equation (7) is a statement of equilibrium defined over the crack facets, and establishes a relation between the traction and separation along the crack facets. This description is complemented by the contact conditions (Eq. (2)).

2.1 | Reduced Basis Approximation

Next, we introduce the reduced order basis approximations for the inelastic strain, stress and separation fields as:

$$\mu_{ij}(\mathbf{y},t) = \sum_{\alpha=1}^{n} N^{(\alpha)}_{\text{ph}}(\mathbf{y})\mu^{(\alpha)}_{ij}(t) \qquad \mathbf{y}\in\Theta \tag{8a}$$

$$\sigma_{ij}(\mathbf{y},t) = \sum_{\alpha=1}^{n} N^{(\alpha)}_{\text{ph}}(\mathbf{y})\sigma^{(\alpha)}_{ij}(t) \qquad \mathbf{y}\in\Theta \tag{8b}$$

$$\delta_i(\mathbf{y},t) = \sum_{\gamma=1}^{m} N^{(\gamma)}_{\text{sep}}(\mathbf{y})\delta^{(\gamma)}_{i}(t) \qquad \mathbf{y}\in S \tag{8c}$$

where $N^{(\alpha)}_{\text{ph}}$ is the inelastic shape functions, n is the number of reduced order shape functions within the polycrystal domain. $N^{(\gamma)}_{\text{sep}}$ is the separation (crack) shape function, and m is the number of reduced order shape functions along the crack facets. $\boldsymbol{\sigma}$ is the Cauchy stress ($\boldsymbol{\sigma} = \mathbf{L} : [\boldsymbol{\epsilon} - \boldsymbol{\mu}]$). The inelastic strain coefficient $\boldsymbol{\mu}^{(\alpha)}$, the stress coefficient $\boldsymbol{\sigma}^{(\alpha)}$ and the separation coefficient $\boldsymbol{\delta}^{(\gamma)}$ are expressed using the non-local weighting functions as:

$$\mu^{(\alpha)}_{ij}(t) = \int_{\Theta} \psi^{(\alpha)}_{\text{ph}}(\mathbf{y})\mu_{ij}(\mathbf{y},t)d\mathbf{y} \tag{9a}$$

$$\sigma^{(\alpha)}_{ij}(t) = \int_{\Theta} \psi^{(\alpha)}_{\text{ph}}(\mathbf{y})\sigma_{ij}(\mathbf{y},t)d\mathbf{y} \tag{9b}$$

$$\delta^{(\gamma)}_{i}(t) = \int_{S} \psi^{(\gamma)}_{\text{sep}}(\mathbf{y})\delta_{i}(\mathbf{y},t)d\mathbf{y} \tag{9c}$$

Following a similar procedure to those outlined in [31] for visco-plasticity alone and in [3] for fracture alone, Eqs. (6) and (7) are expressed in a reduced form for the combined system as:

$$M^{(\alpha)}_{ijkl}\dot{\sigma}^{(\alpha)}_{kl}(t) - \sum_{\beta=1}^{n}(P^{(\alpha\beta)}_{ijkl} - \delta^{(\alpha\beta)}I_{ijkl})\dot{\mu}^{(\beta)}_{kl}(t) - \sum_{\gamma=1}^{m} R^{(\alpha\gamma)}_{ijm}\dot{\delta}^{(\gamma)}_{m}(t) = A^{(\alpha)}_{ijkl}\dot{\bar{\epsilon}}_{kl}(t) \tag{10}$$

$$\dot{t}^{(\gamma)}_{p}(t) + C^{(\gamma)}_{pmn}\dot{\bar{\epsilon}}_{mn}(t) + \sum_{\eta=1}^{m} D^{(\gamma\eta)}_{pm}\dot{\delta}^{(\eta)}_{m}(t) + \sum_{\alpha=1}^{n} T^{(\gamma\alpha)}_{pmn}\dot{\mu}^{(\alpha)}_{mn}(t) = 0 \tag{11}$$

where $\delta^{(\alpha\beta)}$ is the Kronecker delta, $\mathbf{M}^{(\alpha)}$, $\mathbf{P}^{(\alpha\beta)}$, $\mathbf{R}^{(\alpha\gamma)}$, $\mathbf{A}^{(\alpha)}$, $\mathbf{C}^{(\gamma)}$, $\mathbf{D}^{(\gamma\eta)}$ and $\mathbf{T}^{(\gamma\alpha)}$ are collectively called coefficient tensors that are functions of the influence functions. Expressions for the coefficient tensors are listed in the Appendix A.

The system of reduced order equations are closed by representing the crack contact conditions using the separation coefficients $\boldsymbol{\delta}^{(\gamma)}$ and introducing the evolution equations for the inelastic strain coefficients $\boldsymbol{\mu}^{(\alpha)}$. Expressions of contact conditions and evolution equations depend on the shape functions for cracks and phases, the choice of which is further discussed below.

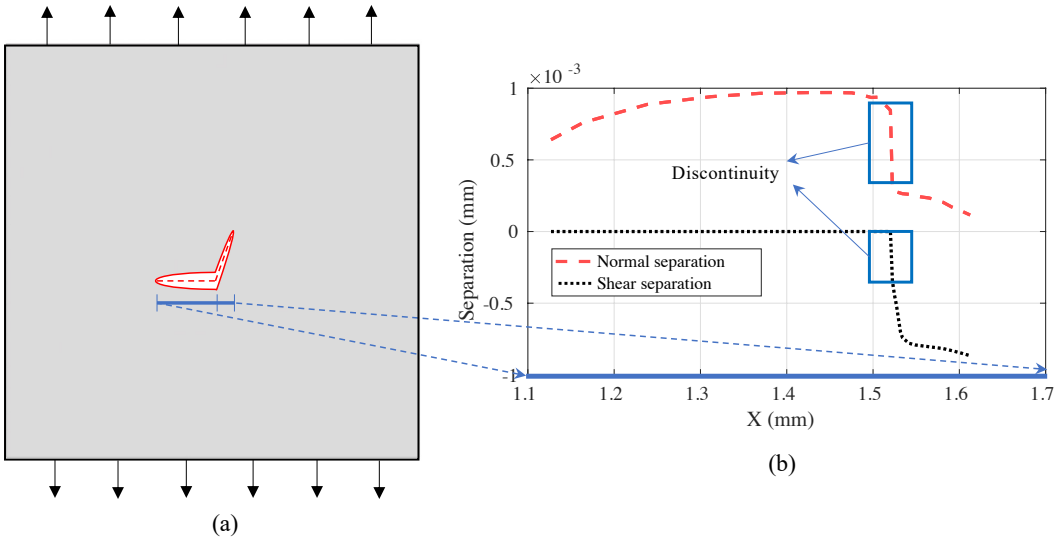

Figure 2 Discontinuity in separation fields: (a) a kinked crack in a 2D microstructure loaded in tension; and (b) normal and shear separations along the crack (x axis)

3 | REDUCED BASIS CONSTRUCTION FOR SHORT CRACKS

Figure 2 (a) illustrates the separation field along a kinked crack within a single-crystal simulated using CPFE. It is observed in Fig. 2 (b) that at the junction point, both the normal and shear components of the separation field show discontinuity. The existence of the component-wise discontinuity of the separation fields requires special treatment of the reduced basis construction. The objective is to identify a set of basis functions that approximates crack opening profile reasonably well under a range of loading conditions. This is particularly critical in multiscale simulations, where volumes associated with different points in a structural domain experience different load histories.

In this section, we discuss the construction of the separation shape functions $N^{(\gamma)}_{\text{sep}}$ and the corresponding weighting functions $\psi^{(\gamma)}_{\text{sep}}$ using a geometry-based domain partitioning strategy. A schematic illustration of the proposed strategy for a kinked crack with two straight segments is shown in Fig. 3. The kinked crack consists of n_{seg} segments distinguished by $n_{\text{seg}} - 1$ junction points. Let $\hat{S}^{(i)}$ denote the domain of the i^{th} segment. At each junction point, a small region denoted as $\hat{S}^{(i,i+1)}$ is introduced, the

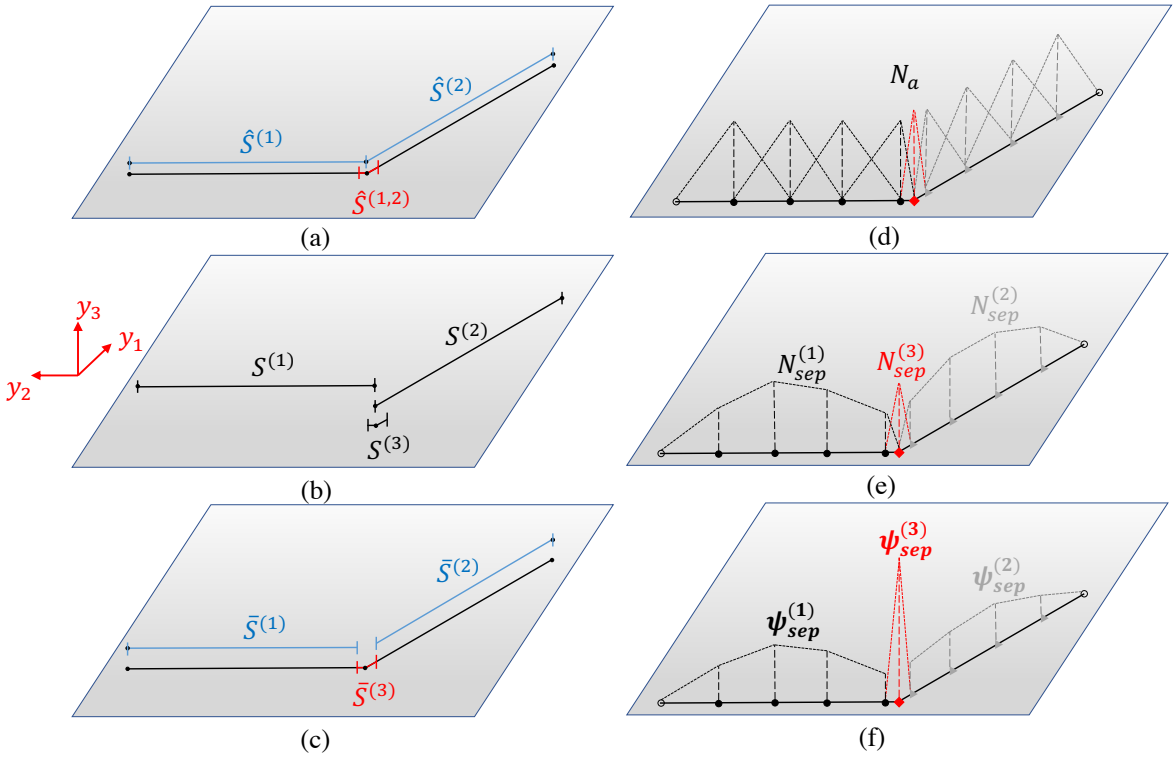

Figure 3 Domain definitions, shape functions and weighting functions: (a) segments $\hat{S}^{(i)}$ and junction regions $\hat{S}^{(i,i+1)}$; (b) overlapping domains $S^{(\gamma)}$; (c) non-overlapping domains $\bar{S}^{(\gamma)}$; (d) finite element shape functions N^a; (e) separation shape functions $N_{\text{sep}}^{(\gamma)}$; and (f) separation weighting functions $\psi_{\text{sep}}^{(\gamma)}$

size of which ($|\hat{S}^{(i,i+1)}| \leq \epsilon$) is small relative to segment sizes (Fig. 3 (a)). Considering the following partitioning (Fig. 3 (b)):

$$S^{(\gamma)} = \hat{S}^{(\gamma)}, \quad \gamma = 1, ..., n_{\text{seg}} \tag{12}$$

$$S^{(\gamma+n_{\text{seg}})} = \hat{S}^{(\gamma,\gamma+1)}, \quad \gamma = 1, ..., n_{\text{seg}} - 1 \tag{13}$$

the support of a shape function is defined based on the corresponding part as:

$$N_{\text{sep}}^{(\gamma)}(\mathbf{y}) = 0 \quad \text{when} \quad \mathbf{y} \in \overline{S \cap S^{(\gamma)}}; \quad \gamma = \{1, ..., m\} \tag{14}$$

where, $m = 2n_{\text{seg}} - 1$. The support for the weighting function is defined by a non-overlapping domain partitioning ((Fig. 3 (c)):

$$\bar{S}^{(1)} = \hat{S}^{(1)}; \quad \bar{S}^{(n_{\text{seg}})} = \hat{S}^{(n_{\text{seg}})} \tag{15a}$$

$$\bar{S}^{(\gamma)} = \hat{S}^{(\gamma)} - \hat{S}^{(\gamma,\gamma+1)} - \hat{S}^{(\gamma-1,\gamma)}, \quad \gamma = 2, ..., n_{\text{seg}} - 1 \tag{15b}$$

$$\bar{S}^{(\gamma+n_{\text{seg}})} = \hat{S}^{(\gamma,\gamma+1)}, \quad \gamma = 1, ..., n_{\text{seg}} - 1 \tag{15c}$$

such that:

$$\psi_{\text{sep}}^{(\gamma)}(\mathbf{y}) = 0 \quad \text{when} \quad \mathbf{y} \in \overline{S \cap \bar{S}^{(\gamma)}}; \quad \gamma = \{1, ..., m\} \tag{16}$$

3.1 | Separation shape and weighting functions

The separation shape functions are expressed based on a finite element discretization using surface (for quasi-2D) or line elements (for 2D) along the crack facets as illustrated in Fig. 3 (d).

$$N_{\text{sep}}^{(\gamma)}(\mathbf{y}) = \sum_{a \in d^{(\gamma)}} \omega^{(\gamma),a} N^a(\mathbf{y}), \qquad \mathbf{y} \in S^{o,(\gamma)} \tag{17}$$

in which $S^{o,(\gamma)}$ denotes the interior of $S^{(\gamma)}$. N^a and $\omega^{(\gamma),a}$ are the finite element shape functions and the corresponding weights associated with node a in $S^{o,(\gamma)}$. $d^{(\gamma)}$ denotes the set of all nodes in $S^{o,(\gamma)}$. The corresponding weighting function is taken to be

of the form:

$$\psi_{\text{sep}}^{(\gamma)}(\mathbf{y}) = \zeta^{(\gamma)} N_{\text{sep}}^{(\gamma)}(\mathbf{y}), \qquad \mathbf{y} \in \bar{S}^{(\gamma)} \tag{18}$$

in which $\zeta^{(\gamma)}$ is a constant. To ensure the consistency of the formulation, the weighting function has to satisfy orthonormality, positivity and normality conditions[31]:

$$\int_S \psi_{\text{sep}}^{(\gamma)}(\mathbf{y}) N_{\text{sep}}^{(\eta)}(\mathbf{y}) d\mathbf{y} = \delta^{(\gamma\eta)}; \tag{19a}$$

$$\psi_{\text{sep}}^{(\gamma)}(\mathbf{y}) \geq 0; \tag{19b}$$

$$\int_S \psi_{\text{sep}}^{(\gamma)}(\mathbf{y}) d\mathbf{y} = 1 \tag{19c}$$

Substituting Eqs. (16) and (18) into Eq. (19a), it is straightforward to see that the orthonormality conditions is achieved by setting:

$$\zeta^{(\gamma)} = \left[\int_{\bar{S}^{(\gamma)}} \left(N_{\text{sep}}^{(\gamma)}(\mathbf{y}) \right)^2 d\mathbf{y} \right]^{-1} \tag{20}$$

The positivity constraint is applied by setting the weights, $\omega^{(\gamma),a}$ to be non-negative. To satisfy normality condition, substituting Eqs. (18) and (20) into Eq. (19c) yields:

$$\int_{\bar{S}^{(\gamma)}} N_{\text{sep}}^{(\gamma)}(\mathbf{y}) d\mathbf{y} = \int_{\bar{S}^{(\gamma)}} \left(N_{\text{sep}}^{(\gamma)}(\mathbf{y}) \right)^2 d\mathbf{y} \tag{21}$$

which is achieved by scaling of the weights, $\omega^{(\gamma),a}$.

3.2 | Identifying the weights for $N_{\text{sep}}^{(\gamma)}$

The description of the separation shape functions $N_{\text{sep}}^{(\gamma)}$ is completed by identifying the weights $\omega^{(\gamma),a}$. We consider two approximations about the crack separation field: (i) the form of crack opening displacements subjected to combined loading can be reasonably described by a linear combination of Mode I (normal) and Mode II (shear) separation functions; and (ii) the Mode II separation field is similar in form to Mode I separation. Under the above approximations, the separation basis function is determined by a linear elastic polycrystalline volume simulation, where the body is subjected to primarily Mode I conditions. The algorithm to obtain the weights that determine the crack opening shape is described as follows:

1. Evaluate the linear response of the polycrystalline volume under pure positive pressure loading:

$$\left\{ L_{ijkl}(\mathbf{y}) u_{(k,y_l)}(\mathbf{y}) \right\}_{,y_j} = - \left\{ L_{ijkk}(\mathbf{y}) \right\}_{,y_j}; \qquad \mathbf{y} \in \Theta \tag{22}$$

2. For each domain $S^{o,(\gamma)}$, $\gamma = \{1, ..., m\}$:

   (a) Loop over each node $a \in d^{(\gamma)}$

   - Compute separation vector in local coordinates

$$\Delta_i^{a,(\gamma)} = R_{ik}^{a,T(\gamma)} \left(u_k^{a,+} - u_k^{a,-} \right) \tag{23}$$

   (b) Loop over each node $a \in d^{(\gamma)}$

   - Compute the weight, $\omega^{(\gamma),a}$ as:

$$\omega^{(\gamma),a} = \frac{\int_{\bar{S}^{(\gamma)}} \sum_{c \in d^{(\gamma)}} \Delta_1^c N^c(\mathbf{y}) d\mathbf{y}}{\int_{\bar{S}^{(\gamma)}} \left\{ \sum_{c \in d^{(\gamma)}} \Delta_1^c N^c(\mathbf{y}) \right\} \left\{ \sum_{b \in d^{(\gamma)}} \Delta_1^b N^b(\mathbf{y}) \right\} d\mathbf{y}} \Delta_1^a \tag{24}$$

in which $\mathbf{R}^{a,(\gamma)}$ denotes the transformation tensor from global to local coordinates defined by the crack normal and $\mathbf{u}^{a,\pm}$ are nodal displacement vectors at the node along the crack. The expansion loading ensures that all cracks within the domain open regardless of their shapes and orientations.

The specific normalization condition in Eq. (24) ensures that the reduced basis functions , $N_{\text{sep}}^{(\gamma)}$ and the corresponding weighting functions, $\psi_{\text{sep}}^{(\gamma)}$ satisfy orthonormality, positivity and normality. A schematic illustration of the resulting separation shape functions and weighting functions are shown in Fig. 3 (e) and (f), respectively.

3.3 | Separation influence function problem

The coefficient tensors that appear in the reduced order model equations are constructed using the elastic influence function $\mathbf{H}(\mathbf{y})$, the inelastic (or phase) influence function $\mathbf{h}^{\text{ph}}(\mathbf{y},\hat{\mathbf{y}})$ and the separation influence function $\mathbf{h}^{\text{sep}}(\mathbf{y},\hat{\mathbf{y}})$. The numerical evaluation of the influence functions have been previously reported (see [53] for $\mathbf{H}$ and [42] for $\mathbf{h}^{\text{ph}}$ and $\mathbf{h}^{\text{sep}}$). Direct computation and memory storage of $\mathbf{h}^{\text{ph}}(\mathbf{y},\hat{\mathbf{y}})$ where $\mathbf{y},\hat{\mathbf{y}} \in \Theta$ and $\mathbf{h}^{\text{sep}}(\mathbf{y},\hat{\mathbf{y}})$ where $\mathbf{y} \in \Theta$ and $\hat{\mathbf{y}} \in S$ are costly, and strictly speaking not necessary as only their integrated forms are employed in the reduced order model in the form of the coefficient tensors. Ref. [31] proposed an approach that directly compute an integrated form of the phase influence function. In this section, we present an approach to efficiently compute an integrated form of the separation influence function.

The separation influence function problem is stated as follows. For a fixed $\hat{\mathbf{y}} \in S$ [42]:

$$\left\{ L_{ijmn}(\mathbf{y}) h^{\text{sep}}_{(m,n)p}(\mathbf{y},\hat{\mathbf{y}}) \right\}_{,y_j} = 0; \quad \mathbf{y} \in \Theta \tag{25}$$

subjected to:

$$Q_{ji}[\![h^{\text{sep}}_{jp}]\!](\mathbf{y},\hat{\mathbf{y}}) = \delta_{ip}\delta(\mathbf{y}-\hat{\mathbf{y}}) \tag{26}$$

where $\mathbf{Q}$ is the transformation from crack local coordinate system to the global coordinate system (i.e., $\mathbf{Q} = \mathbf{R}^T$). By construction explained in the previous section, each of the separation basis functions, $N^{(\gamma)}_{\text{sep}}(\hat{\mathbf{y}})$ is non-negative as they are constructed from the normal separation fields, which themselves are non-negative by definition. We define:

$$h^{\text{sep},(\gamma)}_{ip}(\mathbf{y}) := \int_{S^{(\gamma)}} N^{(\gamma)}_{\text{sep}}(\hat{\mathbf{y}}) h^{\text{sep}}_{ip}(\mathbf{y},\hat{\mathbf{y}}) d\hat{\mathbf{y}} \tag{27}$$

Premultiplying Eqs. (25) and (26) with the separation shape function and integrating over the crack facet, we obtain the following problem for $\mathbf{h}^{\text{sep},(\gamma)}$:

$$\{ L_{ijkl}(\mathbf{y}) h^{\text{sep},(\gamma)}_{(k,y_l)p}(\mathbf{y}) \}_{,y_j} = 0 \qquad \mathbf{y} \in \Theta \tag{28}$$

subjected to:

$$[\![h^{\text{sep},(\gamma)}_{ip}]\!](\mathbf{y}) = Q_{ip} N^{(\gamma)}_{\text{sep}}(\mathbf{y}) \qquad \mathbf{y} \in S \tag{29}$$

From Eq. (27), the selected reduced order shape functions and weighting functions, and the definition of coefficient tensor $\mathbf{R}^{(\alpha\gamma)}$ (Eq. (A4)), it is possible to directly evaluate $\mathbf{R}^{(\alpha\gamma)}$ as:

$$R^{(\alpha\gamma)}_{ijm} = \int_{\Theta} \psi^{(\alpha)}_{\text{ph}}(\mathbf{y}) h^{\text{sep},(\gamma)}_{(i,y_j)m}(\mathbf{y}) d(\mathbf{y}) \tag{30}$$

The following relations stand as $|S^{(\gamma)} - \bar{S}^{(\gamma)}| < \epsilon \ll 1$ for regions other than the junction regions :

$$\lim_{\epsilon\to 0} \int_{\bar{S}^{(\gamma)}} N^{(\gamma)}_{\text{sep}}(\hat{\mathbf{y}}) h^{\text{sep}}_{ip}(\mathbf{y},\hat{\mathbf{y}}) d\hat{\mathbf{y}} \approx \int_{S^{(\gamma)}} N^{(\gamma)}_{\text{sep}}(\hat{\mathbf{y}}) h^{\text{sep}}_{ip}(\mathbf{y},\hat{\mathbf{y}}) d\hat{\mathbf{y}} = h^{\text{sep},(\gamma)}_{ip}(\mathbf{y}) \tag{31}$$

From Eqs. (A6)-(A8), consider that the coefficient tensors $\mathbf{C}^{(\gamma)}$, $\mathbf{D}^{(\gamma\eta)}$ and $\mathbf{T}^{(\gamma\alpha)}$ are integrated over the non-overlapping domain $\bar{S}^{(\gamma)}$ due to the supporting domain of the separation weighting function $\psi^{(\gamma)}_{\text{sep}}$. It is then straightforward to have the following relations satisfied from Eq. (31):

$$C^{(\gamma)}_{pmn} \approx \zeta^{(\gamma)} \int_{\Theta} h^{\text{sep},(\gamma)}_{(i,y_j)p}(\mathbf{y}) L_{ijkl}(\mathbf{y}) A_{klmn}(\mathbf{y}) d\mathbf{y} \tag{32}$$

$$D^{(\gamma\eta)}_{pm} \approx \zeta^{(\gamma)} \int_{\Theta} h^{\text{sep},(\gamma)}_{(i,y_j)p}(\mathbf{y}) L_{ijkl}(\mathbf{y}) h^{\text{sep},(\gamma)}_{(k,y_l)m}(\mathbf{y}) d\mathbf{y} \tag{33}$$

$$T^{(\gamma\alpha)}_{pmn} \approx \zeta^{(\gamma)} \int_{\Theta} h^{\text{sep},(\gamma)}_{(i,y_j)p}(\mathbf{y}) L_{ijkl}(\mathbf{y}) S^{(\alpha)}_{klmn}(\mathbf{y}) d\mathbf{y} \tag{34}$$

As shown in Fig. 3, we introduce nodes immediate to the junction points such that the difference between $S^{(\gamma)}$ and $\bar{S}^{(\gamma)}$ is sufficiently small and the above approximations are reasonable. For junction regions (or straight cracks with no kinks), the above approximation becomes equality conditions since $\bar{S}^{(\gamma)} = S^{(\gamma)}$.

4 | REDUCED BASIS CONSTRUCTION FOR THE PHASES

In this section, we focus our attention on the phase partitioning strategy. Considering the partitioning of the polycrystalline volume Θ into n non-overlapping subdomains $\Theta^{(\alpha)}$ ($\Theta = \bigcup_{\alpha=1}^{n} \Theta^{(\alpha)}$ and $\Theta^{(\alpha)} \cap \Theta^{(\beta)} = \emptyset$ for $\alpha \neq \beta$). The shape and weighting functions are then chosen as in Ref.[31]:

$$N_{\text{ph}}^{(\alpha)}(\mathbf{y}) = \begin{cases} 1, & \mathbf{y} \in \Theta^{(\alpha)} \\ 0, & \mathbf{y} \notin \Theta^{(\alpha)} \end{cases}; \qquad \psi_{\text{ph}}^{(\alpha)}(\mathbf{y}) = \frac{1}{|\Theta^{(\alpha)}|} N_{\text{ph}}^{(\alpha)} \tag{35}$$

Equation (35) indicates that the phase shape and weighting functions are piece-wise constant within each subdomain $\Theta^{(\alpha)}$, making stress and strain (or any other field variables) in the reduced order system stay constant in each subdomain as well. In the presence of cracks, high stress and strain concentrations, and high stress gradients occur around the crack tips. A partitioning strategy that uses large number of reduced order parts around the crack tips are therefore necessary to capture the stress or strain concentrations with reasonable accuracy.

The existing partitioning strategies can be generally classified into two categories: (1) geometry-based strategy [54,55,56,57,58] uses internal features such as grains in the polycrystalline microstructures or inclusions in the particulate composites to define the partitions; and (2) response-based strategy[43,44,59,60,61] groups the subdomains of the microstructure with similar responses into the same parts when the microstructure is subjected to a given loading. In this work, we propose a mixed approach: The partitioning is initiated by ensuring that each grain in the polycrystalline volume is represented by at least one part (i.e., $n \geq n_{\text{grain}}$). During the simulation performed to construct the crack shape functions (Section 3.2), an energy-like quantity is calculated within the volume and used to group subdomains of each grain for further partitioning.

Let e_k^i denote the k^{th} finite element in the i^{th} grain within the polycrystalline volume, $e^i = \left\{ e_k^i \mid k = 1, ..., n_i \right\}$ the list of all elements in grain i, E_k^i the energy measure computed at the k^{th} finite element in i^{th} grain, $E^i = \left\{ E_k^i \mid k = 1, ..., n_i \right\}$ the list of all energy values in grain i, and n_i the number of elements in the i^{th} grain. The algorithm used for phase partitioning consists of the following steps:

1. Evaluate the linear response of the polycrystalline volume subjected to expansion loading as described by Eq. (22).
2. Compute the energy measure for each element, $k = 1, ..., n_i$ of each grain, $i = 1, ..., n_{\text{grain}}$
$$E_k^i = L_{ijkl}^{e_k^i} u_{(i,y_j)}^{e_k^i} u_{(k,y_l)}^{e_k^i} \tag{36}$$
3. Find the maximum energy value among all elements and normalize the energy values
$$E_{max} = \max\{ E_k^i \mid i = 1, ..., n_{\text{grain}}; k = 1, ..., n_i \} \tag{37}$$
$$E_k^i = \frac{E_k^i}{E_{max}}; \quad i = 1, ..., n_{\text{grain}}; \quad k = 1, ..., n_i \tag{38}$$
4. Define an equally spaced array $\mathbf{A} = [a_0, ..., a_{n_{\text{space}}}]$ such that
$$a_j - a_{j-1} = \frac{1}{n_{\text{space}}}; \quad j = 1, ..., n_{\text{space}} \tag{39}$$
where n_{space} is an input parameter.
5. Loop over each grain i
   (a) Sort the elements in grain i (e^i) based on normalized energy values in the ascending order to obtain $\hat{e}^i$ (along with the corresponding sorted energies, $\hat{E}^i$)
   (b) Assign each element $\hat{e}_k^i$ to an element set Θ_l^i based on its normalized energy value such that: $\Theta_l^i := \left\{ \hat{e}_k^i \mid a_l < \hat{E}_k^i \leq a_{l+1} \right\}$. The resulting set Θ_l^i means the l^{th} subdomain (or part) in i^{th} grain.
6. Reindex Θ_i^l to obtain $\Theta^{(\alpha)}$

The proposed algorithm is a straightforward approach to group subdomains of grains with similar energies into reduced order parts. The resulting parts do not necessarily have topological connectivity, but the material points within a part are assumed to undergo similar deformation. Sorting of the energy (Step 5(a)) is performed to more efficiently assign elements to the correct

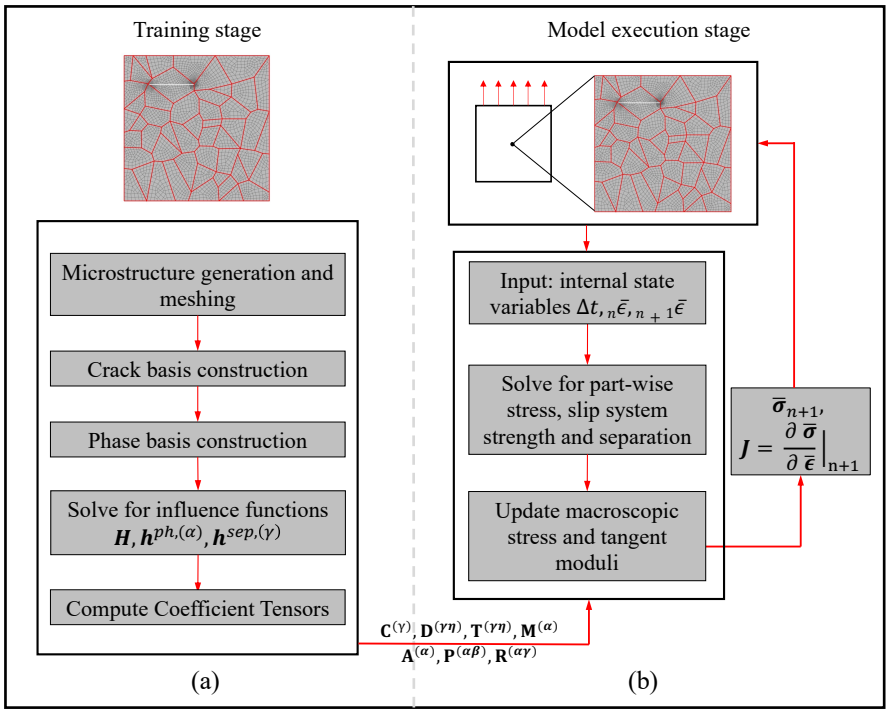

Figure 4 Implementation strategy for the reduced order problem: (a) model construction and (b) model execution

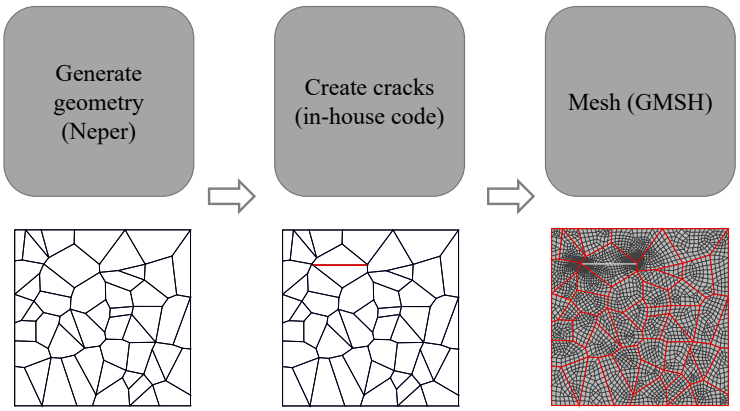

Figure 5 Finite element mesh creation procedures used in the training stage of the reduced order model

element set (Θ_l^i). It is also worthy to note that many of the element sets Θ_l^i are null (i.e., none of the values fall in the range of Θ_l^i). These element sets are eliminated in the reindexing step (Step 6). Naturally, the number of parts produced with this algorithm increases with n_{space}, and $n = n_{\text{grain}}$ if n_{space} is set to 1.

Remark

Although we demonstrate the clustering algorithm in the context of terminating the crack at the grain boundaries, it is flexible to be extended to sub-grain cracking in which the crack is fully contained within certain grain. One could split the grain where the crack resides into several smaller parts with the same orientation, and let the crack split one of the small parts such that it does not split the entire grain at once. The clustering algorithm is agnostic to such extra splitting and can still deliver refined partition around the crack tips.

5 | NUMERICAL IMPLEMENTATION

As shown in Fig. 4, the implementation of the proposed model consists of two steps: training (or model construction) and model execution. The training stage involves microstructure generation and meshing, crack basis function construction, phase basis function construction, influence function computation, and numerical integration to obtain the coefficient tensors (Fig. 4 (a)). We use Neper[62] software to generate the microstructure geometry without cracks. An in-house Matlab code modifies the geometry to insert the cracks by splitting the grain. Finally, the modified geometry is meshed by GMSH[63]. The polycrystalline volume creation process is illustrated in Fig. 5. This procedure results in cracks that terminate at the grain boundaries. It is straightforward to extend the procedure to cases where the crack tip is within a grain. This could be done by splitting the grain into smaller grains with the same orientation, and letting the crack terminate at the boundary of the smaller grains. The crack and phase basis function constructions follow the procedures as described in Sections 3 and 4. The influence function and coefficient tensor computation can be found in in[31,42], and are omitted here for brevity.

The model execution stage is summarized in Fig. 4 (b). The driving strain is generated by solving a macroscale equilibrium problem defined over a single hexahedral element[31]. Given the driving strain at the last increment and current increment, ${}_n\bar{\boldsymbol{\epsilon}}$ and ${}_{n+1}\bar{\boldsymbol{\epsilon}}$, and the time increment Δt, the reduced order system of equations (i.e., Eq. (10), Eq. (11) and the evolution equations) are evaluated as the constitutive update to obtain part-wise stresses, slip system strength and separations as three sets of unknowns at each quadrature point. The stress and tangent moduli at current increment are then computed and passed back to the macroscale finite element solver. The open-source finite element package CACULIX is used as the macroscale solver. The reduced order system of equations are solved within the user supplied subroutine (UMAT).

6 | NUMERICAL VERIFICATION

The proposed reduced order model is verified against crystal plasticity finite element simulations, where the microstructure features are fully resolved. The verification studies were performed on quasi-2D microstructures made up of equiaxed hexagonal close packed (HCP) crystals with random texture. Grain orientations are sampled from a uniform distribution. In reference CPFE simulations and in computing the influence functions of the ROM, the microstructure domain is discretized using hexahedral finite elements that conform to the grain boundaries. In influence function calculations, periodic boundary conditions are applied on the two in-plane directions (i.e., x and y) and free boundary condition is applied on the out-of-plane direction (i.e., z). A dislocation density based crystal plasticity model is employed to describe the crystallographic slip and hardening evolution. The model parameters are set to represent the behavior of the titanium alloy, Ti-6242S and summarized in Table B1 in Appendix B. The model is briefly introduced in Appendix B. Detailed description of the model is provided in Ref[33].

6.1 | Assessment of the partitioning algorithm

The robustness of the partitioning algorithm proposed in Section 4 is demonstrated in this section. Figure 6 (a) and (b) show the polycrystalline geometry, grain orientations and discretizations of a 50-grain microstructure with a straight crack (white line in Fig. 6 (b)). The mesh is refined near the crack tips. Figure 6 (c) shows the reduced order phase partitioning obtained by setting $n_{\text{space}} = 40$, resulting in $n_{\text{parts}} = 200$. Near the crack tips, the reduced order parts are more refined, and the regions away from the crack tips are less refined.

Figure 7 shows the relationship between the parameter, n_{space} and the resulting ROM order. The figures shows a roughly linear relationship between n_{space} and n_{parts}. When $n_{\text{space}} = 1$, the number of ROM parts is equal to the number of grains. The effect of the mesh density on the resulting ROM identification is investigated by discretizing the microstructure shown in Fig. 6 (a) with three mesh densities, where the total number of elements for the three cases are $10,852$, $16,902$ and $21,916$. For all three cases, n_{space} is set to 40. The mesh refinements particularly increase the number of elements around the crack tips. The number of ROM parts for the three cases remain approximately 200, demonstrating that the selection of the underlying mesh does not affect the ROM provided that the mesh is fine enough to discretize the stress and strain concentrations induced by the short cracks.

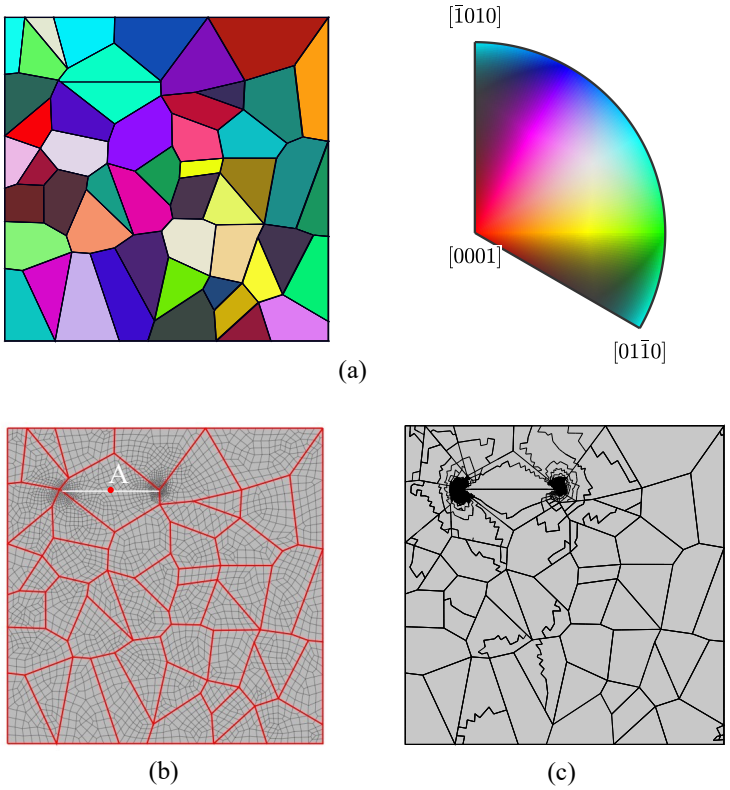

Figure 6 (a) Microstructure geometry and texture (color of grains represents position on the inverse pole figure); (b) mesh (white line denotes the crack); and (c) partitioning scheme from the partitioning algorithm

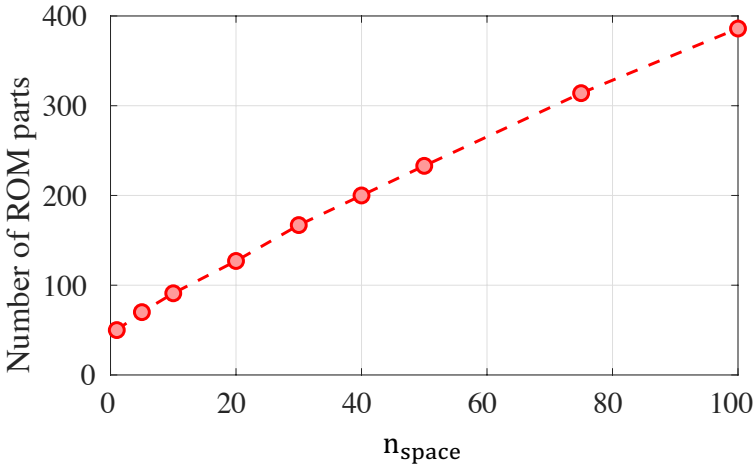

Figure 7 Number of ROM parts as a function of n_{space}

6.2 | Effects of model complexity

In this section, we demonstrate how model complexity affects the ROM accuracy. The relative complexity is defined as the ratio between the degrees of freedom of the ROM (DoF_{ROM}) and the reference CPFE model (DoF_{CPFE}). $\text{DoF}_{\text{CPFEM}} = 63,000$ for the reference model shown in Fig. 6 (b), whereas $\text{DoF}_{\text{ROM}} = 6\text{n} + 3\text{m}$. Given that a single straight crack is considered, a single

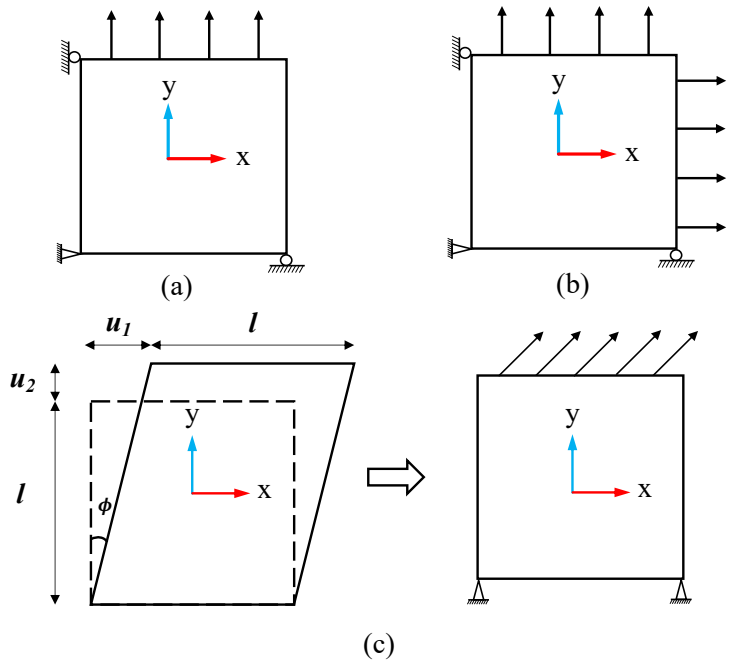

Figure 8 Boundary conditions (a) for uniaxial loading; (b) for biaxial loading; and (c) for stress-envelope construction. Symmetry boundary conditions are applied in the out-of-plane direction

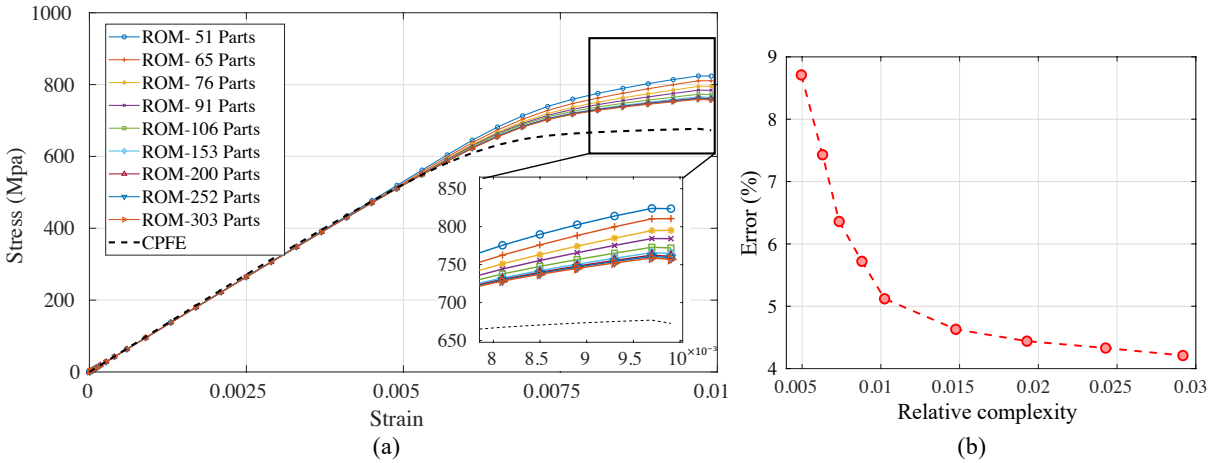

Figure 9 (a) Stress-strain curves of different numbers of ROM parts; and (b) Model error as a function of model complexity

separation function is used ($m = 1$). The error measure proposed in [31] is used:

$$\text{Error} = \int \frac{|\sigma_{\text{ROM}} - \sigma_{\text{CPFE}}|}{|\sigma_{\text{CPFE}}|} d\epsilon \tag{40}$$

where σ_{ROM} and σ_{CPFE} are the macroscopic engineering stress components along the direction of interest (e.g., loading direction). The model error is then assessed using Eq. (40) when the microstructure is subjected to the boundary conditions shown in Fig. 8 (a). A monotonic uniaxial tension loading is applied in the y direction up to 1% strain at the rate of $0.01/s$. The stress-strain curves and the model error as functions of model complexity are plotted in Fig. 9 (a) and (b), respectively. As the number of ROM parts increases, the crack tip regions are more refined, and the high stress gradients in those regions are captured more accurately. This local accuracy improvement is reflected in the improvement of the overall stress-strain curve as well (Fig. 9 (a)).

The most refined ROM in this study consists of $n_{\text{part}} = 303$ and has relative complexity of approximately 3%. The rate of model accuracy improvement gradually reduces with increased model complexity and appears to asymptote to an error magnitude of approximately 4%. This residual error is attributed to the inability of the influence functions (hence the coefficient tensors) computed using elastic moduli of the grains to fully capture the local deformation behavior. This issue has been studied in[64,65] particularly for low order ROMs, but remains outstanding in the context of polycrystalline microstructures.

6.3 | Kinematics near the crack

The verification of the ROM's ability to capture the crack separation behavior as a function of loading is investigated using the 200-part ROM shown in Fig. 6. This ROM is chosen because further increase in the ROM order does not significantly increase accuracy as demonstrated in Fig. 9 (b). The microscopic domain is subjected to the boundary conditions as shown in Fig. 8 (a). Strain controlled cyclic uniaxial loading is applied up to 1% strain with R-ratio $= -1$ and at 0.04/s strain rate. The overall (i.e., macroscopic) stress-strain curve, along with the traction-macroscopic strain and traction-separation curves predicted by the ROM and CPFE models are compared in Fig. 10. The plotted traction and separation histories are the normal components of the traction and separation coefficients ($t_N^{(1)}$ and $\delta_N^{(1)}$, respectively, noting that $m = 1$) that correspond to the point along the crack that exhibits the largest values of peak separation. This point is shown as point "A" in Fig. 6 (b). We note that both CPFE and ROM predict the same spatial point for peak separation even after the onset of plasticity. The deformation process can be described as follows: as the sample is loaded in tension, the crack opens and the separation increases with the loading until peak tensile strain. The onset of significant crack tip plasticity occurs at approximately 0.5% applied strain beyond which, separation-strain curve begins to deviate from linearity. This increase in rate of change of separation is caused by the localized plastic strains at the crack tips. The ROM slightly underpredicts the peak separation (error=12.09%), but the deviation from linearity is captured by the ROM. As the specimen is unloaded from peak tensile state, the separation gradually reduces. At the unloaded state ($\bar{\epsilon}_{yy} = 0$), compressive macroscopic stress is evident, whereas the separation state of point A remains positive. As the sample is loaded in compression, the crack eventually completely closes and the traction coefficient becomes nonzero while separation stays zero for the remainder of the compression loading and unloading. The traction-strain curve exhibits elastic-plastic behavior consistent with the overall stress-strain response. At the end of the unloading process, the crack reopens and the sample gets into the tension state again.

The separation profiles predicted by the ROM and CPFE are compared in Fig. 11 for four loading stages: (a) peak stress, (b) fully unloaded after tension $\bar{\epsilon}_{yy} = 0$, (c) when traction becomes non-zero, and (d) fully unloaded after compression $\bar{\epsilon}_{yy} = 0$. Overall, a reasonable match is observed between the ROM and CPFE predictions. Particularly at stages (a) and (b), the ROM underestimates the crack tip opening displacement, whereas the maximum separation is predicted with better accuracy. The separation has a rectangular profile for CPFE whereas it is elliptical for ROM. This is because the plastic deformation near the crack tips is significant at these two stages, which affects the separation profile. The crack shape function employed in ROM is obtained under the assumption of fully elastic behavior and does not account for the change in shape of separation profile.

6.4 | Effects of loading conditions

One of the primary advantages of the proposed model is its ability to extrapolate under arbitrary loading conditions once a ROM has been trained, provided that the microstructures remain unchanged. To demonstrate the ROM's extrapolation capability, the cracked microstructure shown in Fig. 6 is subjected to various multiaxial loading conditions generated using the boundary conditions shown in Fig. 8 (c). Figure 12 shows the stress envelope – the equivalent stress as a function of normal and shear strains under monotonic loading. The equivalent stress σ_{eq} considers the normal and shear components of the macroscopic stress tensor: $\sigma_{eq} = \sqrt{\bar{\sigma}_{yy}^2 + \bar{\sigma}_{xy}^2}$. The normal and shear strain in Fig. 12 are defined as $\epsilon = u_2/l$ and $\gamma = \phi \approx \tan(\phi) = u_1/l$, respectively. The stress envelope is constructed by varying the magnitudes of u_1 and u_2 to account for various normal and shear strain combinations with proportional loading, and then observing the evolution of the equivalent stress σ_{eq} as predicted by the ROM and CPFE. The combinations of u_1 and u_2 are generated using: $u_1 = 0.045\cos\left(\pi/2(n_{\text{load}} - 1)i\right)$ and $u_2 = 0.045\sin\left(\pi/2(n_{\text{load}} - 1)i\right)$, where n_{load} is the total number of load cases (n_{load}=19), and $i = 0, ..., n_{\text{load}} - 1$. Under all loading conditions, the ROM shows reasonable match with the CPFE. The largest error (24.34%) in terms of the peak stress in the ROM prediction is observed when the microstructure is loaded in pure shear loading i.e., $(u_1, u_2) = (0.045, 0.)$ and smallest error (7.77%) is observed when $(u_1, u_2) = (0.0258, 0.0323)$. At pure normal loading $(u_1, u_2) = (0., 0.045)$, the error is 10.47%. In all cases, the ROM consistently exhibits a stiffer response compared with the CPFE model, as it constrains the kinematics relative to CPFE.

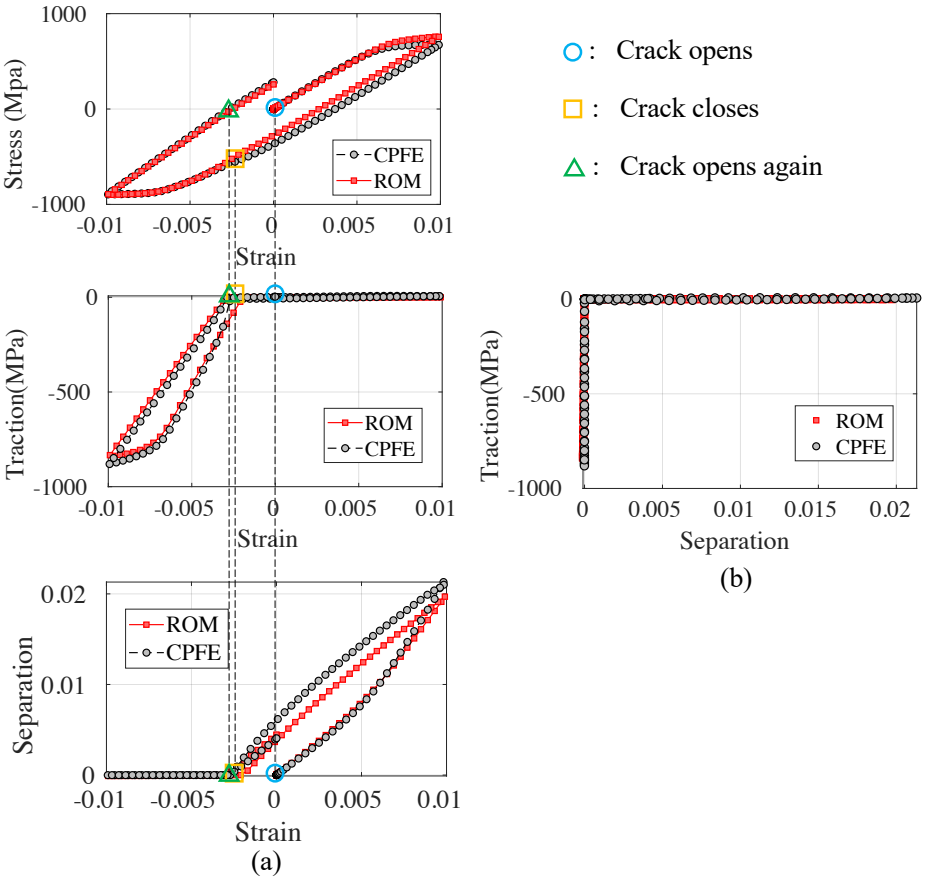

Figure 10 Overall behavior comparison: (a) from top to bottom: engineering stress-strain curve, traction-strain curve and separation-strain curve; and (b) traction-separation curve

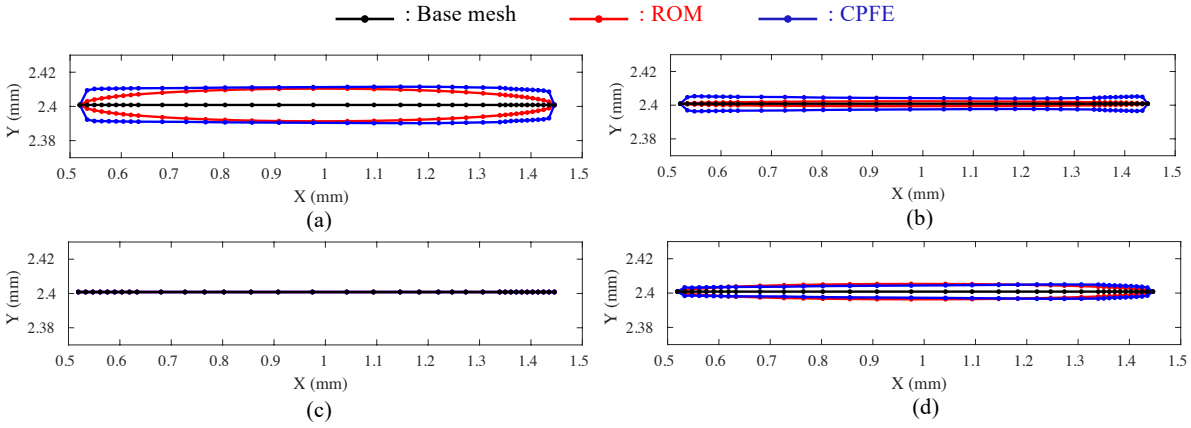

Figure 11 Separation field comparison: (a) at peak stress (scale=1); (b) fully unloaded in tension $\bar{\epsilon}_{yy} = 0$ (scale=1); (c) traction becomes non-zero (scale=1); and (d) fully unloaded in compression $\bar{\epsilon}_{yy} = 0$ (scale=2)

To examine the model performance under additional cyclic loading conditions, the microstructure is subjected to the boundary conditions in Fig. 8 (b). The microstructure is loaded in the y direction cyclically with applied strain up to 1% with R-ratio $= -1$ at constant strain rate of 0.02/s. Simultaneously, a 2% uniaxial and monotonic tensile strain is applied with a constant strain

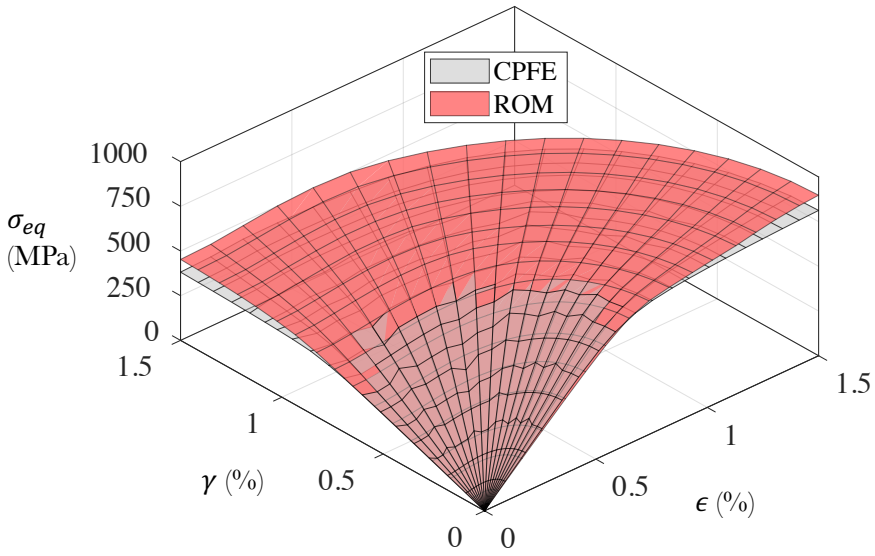

Figure 12 Stress envelopes for ROM and CPFE

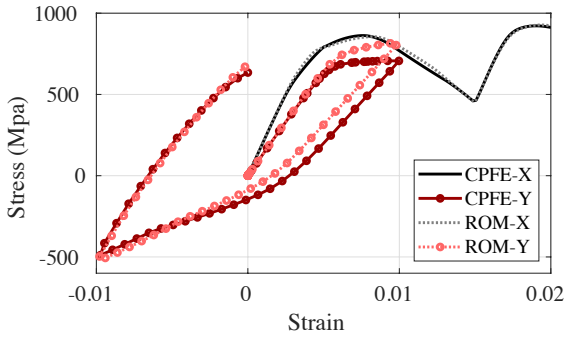

(a)

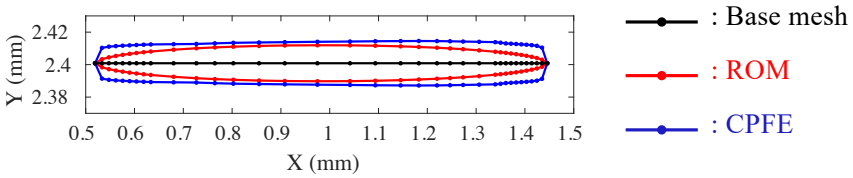

(b)

Figure 13 (a) Stress-strain curve under cyclic biaxial loading; and (b) separation field comparison at peak tensile stress in y direction under cyclic biaxial loading

rate of 0.01/s in the x direction. Figure 13 (a) shows the resulting stress-strain curves. The ROM slightly over-predicts the peak stress in the y direction whereas a better match in the x direction is observed. The separation fields are compared at the peak tensile stress state in y direction as shown in Fig. 13 (b). Similar to that in the uniaxial loading condition, the peak separation (i.e., point A) shows reasonable match between the ROM and CPFE, whereas the ROM underpredicts the separation near the crack tip regions.

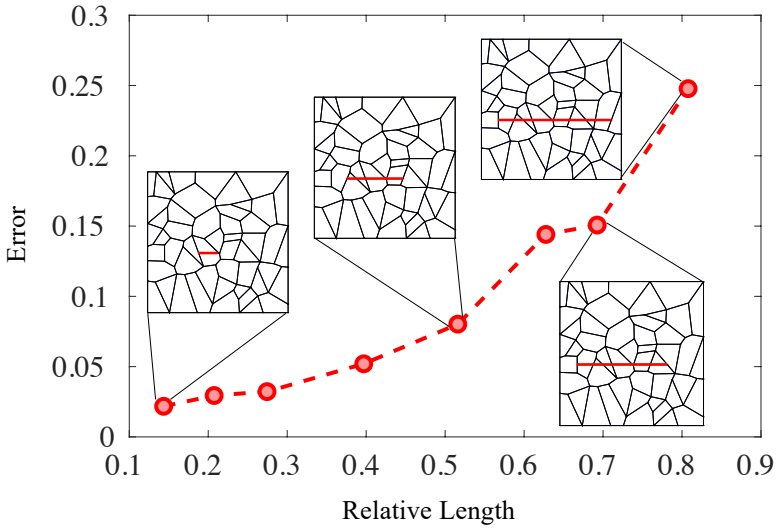

Figure 14 ROM error as a function of crack length: the red lines denote the cracks

6.5 | Effects of crack length

Figure 14 shows the error in ROM predictions relative to CPFE as a function of crack length. The general morphology of the microstructure considered in this study is similar to that discussed in Fig. 6. In each analysis, a crack with relative length l/L (14.4% to 80.8% with l and L respectively the crack and microstructure volume edge length) is embedded in the microstructure. A total of 8 different crack lengths were considered. A change in the crack length changes the resulting reduced order model. A separate ROM is therefore trained for each case. Model orders and the corresponding partitioning parameters n_{space} used to generate Fig. 14 are summarized in Table 1 (n_{space} are selected such that the number of reduced order parts for each ROM is around 200). As the crack grows longer, the ROM error increases. The increasing trend in error is primarily attributed to the interaction between microstructure volume edges and the crack tips as they come closer. This effect is due to the treatment of the boundary conditions of the reference CPFE model and the ROM as described at the beginning of the verification section. While the trend is largely monotonic, the slight variations are due to the variations in the ROM order generated for each crack length. One way to improve the accuracy in the case of longer cracks is to increase the microstructure size since it is the relative length of the crack that dominates the error.

Table 1 Model orders and parameter N for microstructure with different crack length

Model number	1	2	3	4	5	6	7	8
Relative length	0.144	0.207	0.274	0.397	0.516	0.628	0.693	0.808
Model order	201	202	207	205	208	207	204	206
$\mathbf{n}_{\text{space}}$	41	37	37	46	41	35	34	31

6.6 | Assessment of local response

The capability of the proposed ROM to capture the localized response is assessed using a microstructure that consists of four cracks with different orientations. One of the cracks included in the domain is a kinked crack that consists of one junction point (i.e., $m = 3$). The geometry and grain orientations of the base microstructure (i.e., the uncracked microstructure) is the same as those for the base microstructure in Fig. 6 (a). However, since different cracks are considered, a different ROM is trained for this specific microstructure. Figure 15 shows the mesh for this microstructure used in the CPFE analysis and ROM training. Note that immediate nodes are added in the vicinity of the joint node. The boundary conditions in Fig. 8 (a) are used and a

1% monotonic uniaxial tension is applied. There are in total 342 ROM parts generated for this example with the partitioning algorithm parameter, $n_{\text{space}} = 25$.

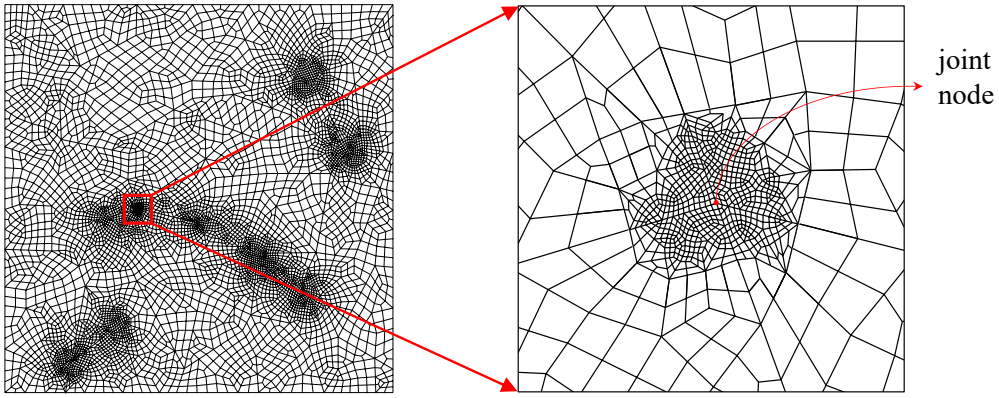

Figure 15 Base mesh of the general cracked microstructure: adding immediate nodes next to the junction node

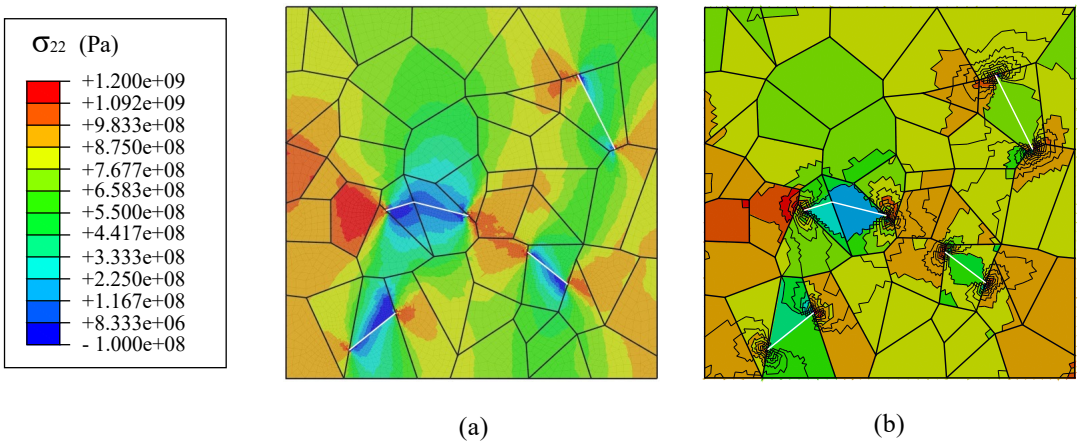

Figure 16 Stress contour comparison: (a) CPFE and (b) ROM

Figure 16 shows the local stress contour plots for the ROM and the reference model at the peak stress, with the white lines representing the cracks. The ROM contour displays piecewise constant stress field as a function of the ROM parts, whereas the CPFE contour is based on the finite element mesh. The ROM captures the stress concentrations around the crack tips with reasonable accuracy, while it over-predicts the stress state at the low stress regions along the crack facets. Figure 17 compares the corresponding strain contours. Naturally, strain concentrations occur at the high stress regions for both of the ROM and the CPFE model. Figure 18 provides a more quantitative comparison of the localized behaviors, where the part-wise stress, strain and dislocation density distributions at the peak load are compared as histogram plots. The part-wise quantities are volume-averaged for each part (as identified in the ROM) in the reference model. The bin plots represent the CPFE results and solid line with dots represent the ROM results. The local distributions are well captured by the ROM for all three quantities. As expected, the crack tip regions exhibit high strain concentration with the remainder of the domain exhibiting relatively low level of strains as evidenced by both contour and histogram plots. The separation fields comparison is shown in Fig. 19. The separation field of ROM in general matches with that of CPFE even when multiple cracks exist in the microstructure, whereas the general shapes of the crack tip opening displacements slightly differ in the same manner described above for the one-crack case. It is noteworthy that at the junction point of the kinked crack, the separation field is well approximated by the proposed model.

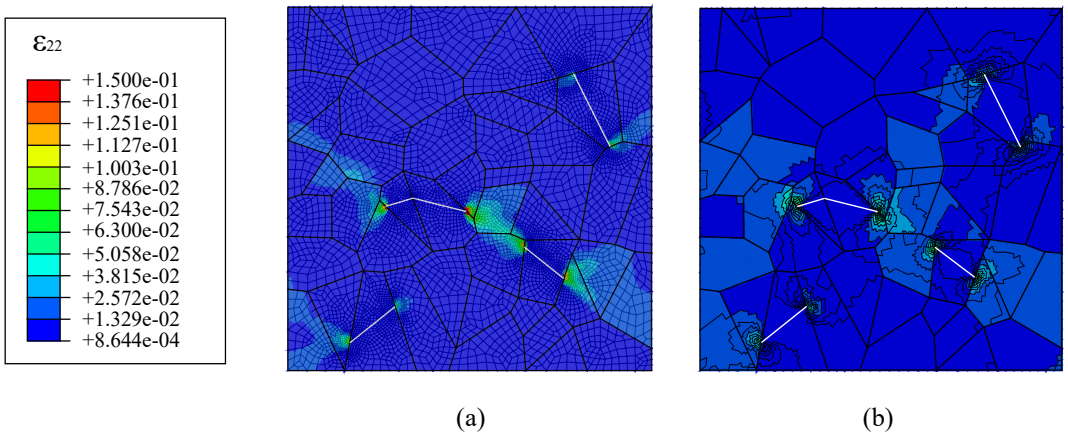

Figure 17 Strain contour comparison: (a) CPFE and (b) ROM

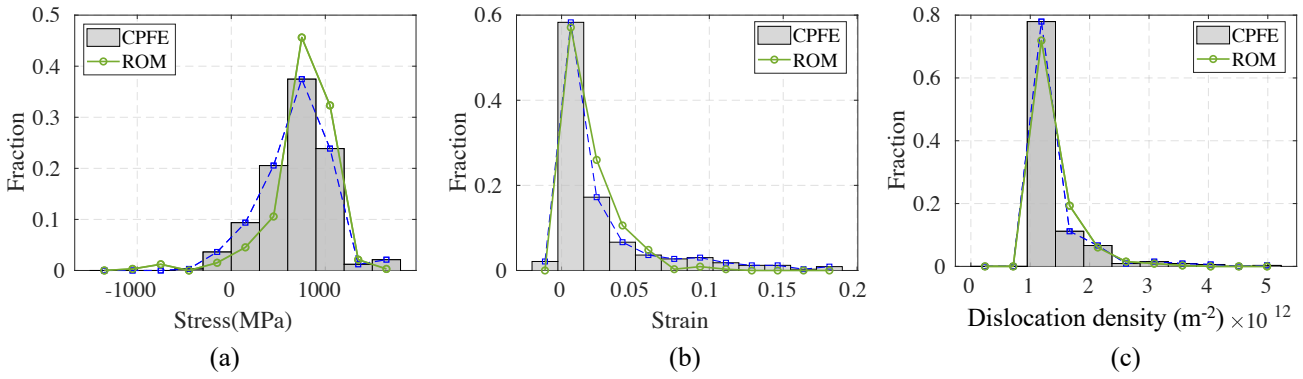

Figure 18 Stress, strain and dislocation density distributions

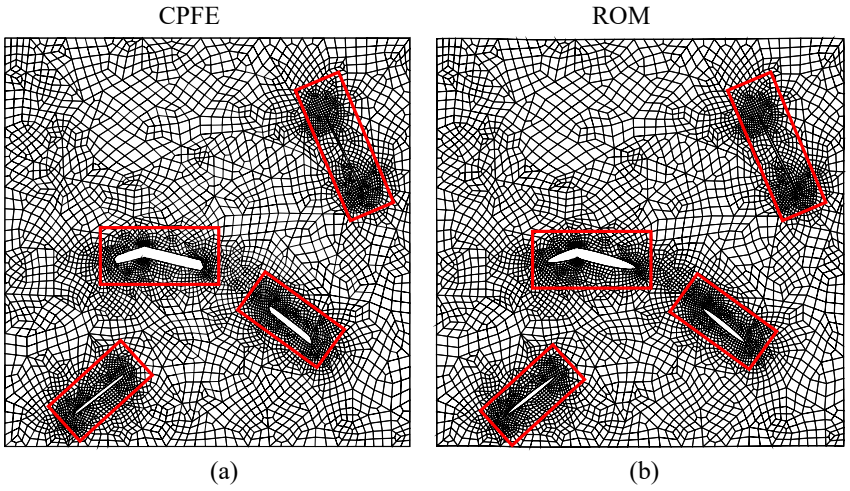

Figure 19 Separation fields comparison at peak tensile stress (cracks are highlight in red box): (a) CPFE; and (b) ROM

To highlight the ROM's ability to capture the high stress regions with good accuracy throughout the loading process, the stress-strain curves for a number of reduced order model parts around the crack tip regions is shown in Fig. 20 when the microstructure

is loaded in monotonic uniaxial tension. All five stress-strain curves show reasonable match with the grain-averaged stress-strain curves obtained using the CPFE simulations.

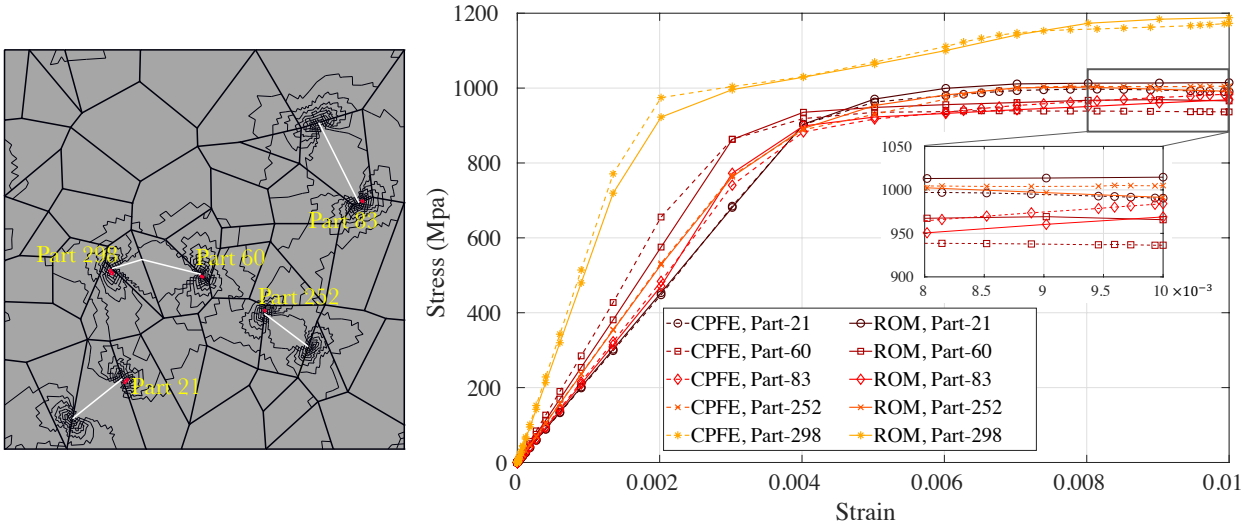

Figure 20 Stress-strain curves for selected parts around the crack tips

7 | CONCLUSIONS AND FUTURE WORKS

This manuscript proposed a novel reduced order homogenization model to predict the mechanical response of 2D and quasi-2D polycrystalline microstructure in the presence of straight and kinked cracks. The proposed approach employs the eigendeformation based homogenization method (EHM) to account for the crystal plasticity and the presence of microstructurally small cracks. Reduced basis construction procedures for the separation fields and the phases are introduced to accurately describe local and global behavior. The reduced order model is verified against crystal plasticity finite element model in terms of various microstructure configurations and loading conditions, both of the overall and local behaviors show reasonable accuracy but with much lower model complexity compared with the reference CPFE simulations. Considering the high computational efficiency of the proposed approach, a possible future application of this study is to incorporate the proposed ROM as a replacement for full-field finite element models in the adaptive crack insertion framework[66] for modeling short crack propagation. This integration could potentially alleviate the computational challenges typically associated with these methods, enabling more efficient modeling of short crack propagation.

The proposed approach has two limitations that will need to be addressed to extend its capabilities. The first is modeling fully 3D microstructures with arbitrarily complex crack morphologies in a computationally efficient fashion. The second is accounting for the evolution of separation field as a function of crack tip plasticity. The results in this manuscript demonstrates that the crack tip opening displacement begin to deviate from CPFE predictions at large local plastic strain.

8 | ACKNOWLEDGMENT

The authors gratefully acknowledge the financial support from the National Aeronautics and Space Administration (NASA), Space Technology Early State Innovation (ESI) Grant (No.:80NSSC20K0294).

References

1. Eylon D, Pierce C. Effect of microstructure on notch fatigue properties of Ti-6Al-4V. *Metallurgical Transactions A* 1976; 7: 111–121.
2. Zhang X, Liu Y, Oskay C. Uncertainty quantification for microstructure-sensitive fatigue nucleation and application to titanium alloy, Ti6242. *Frontiers in Materials* 2022; 9: 897998.
3. Oskay C, Su Z, Kapusuzoglu B. Discrete eigenseparation-based reduced order homogenization method for failure modeling of composite materials. *Computer Methods in Applied Mechanics and Engineering* 2020; 359: 112656.
4. Peirce D, Asaro R, Needleman A. An analysis of nonuniform and localized deformation in ductile single crystals. *Acta Metallurgica* 1982; 30: 1087–1119.
5. Peirce D, Asaro RJ, Needleman A. Material rate dependence and localized deformation in crystalline solids. *Acta Metallurgica* 1983; 31: 1951–1976.
6. Lebensohn RA. N-site modeling of a 3D viscoplastic polycrystal using fast Fourier transform. *Acta Materialia* 2001; 49: 2723–2737.
7. Lebensohn RA, Kanjarla AK, Eisenlohr P. An elasto-viscoplastic formulation based on fast Fourier transforms for the prediction of micromechanical fields in polycrystalline materials. *International Journal of Plasticity* 2012; 32: 59–69.
8. Prakash A, Lebensohn R. Simulation of micromechanical behavior of polycrystals: finite elements versus fast Fourier transforms. *Modelling and Simulation in Materials Science and Engineering* 2009; 17: 064010.
9. Vidyasagar A, Tan WL, Kochmann DM. Predicting the effective response of bulk polycrystalline ferroelectric ceramics via improved spectral phase field methods. *Journal of the Mechanics and Physics of Solids* 2017; 106: 133–151.
10. Rovinelli A, Proudhon H, Lebensohn RA, Sangid MD. Assessing the reliability of fast Fourier transform-based crystal plasticity simulations of a polycrystalline material near a crack tip. *International Journal of Solids and Structures* 2020; 184: 153–166.
11. Bittencourt TN, Wawrzynek P, Ingraffea A, Sousa J. Quasi-automatic simulation of crack propagation for 2D LEFM problems. *Engineering Fracture Mechanics* 1996; 55: 321–334.
12. Li J, Proudhon H, Roos A, Chiaruttini V, Forest S. Crystal plasticity finite element simulation of crack growth in single crystals. *Computational Materials Science* 2014; 94: 191–197.
13. Wilson D, Dunne FP. A mechanistic modelling methodology for microstructure-sensitive fatigue crack growth. *Journal of the Mechanics and Physics of Solids* 2019; 124: 827–848.
14. Kumar S, Singh I, Mishra B, Sharma K, Khan I. A homogenized multigrid XFEM to predict the crack growth behavior of ductile material in the presence of microstructural defects. *Engineering Fracture Mechanics* 2019; 205: 577–602.
15. Luther T, Könke C. Polycrystal models for the analysis of intergranular crack growth in metallic materials. *Engineering Fracture Mechanics* 2009; 76: 2332–2343.
16. Lu M, Wang F, Zeng X, Chen W, Zhang J. Cohesive zone modeling for crack propagation in polycrystalline NiTi alloys using molecular dynamics. *Theoretical and Applied Fracture Mechanics* 2020; 105: 102402.
17. Clayton J, Knap J. Phase field modeling of directional fracture in anisotropic polycrystals. *Computational Materials Science* 2015; 98: 158–169.
18. Arriaga M, Waisman H. Stability analysis of the phase-field method for fracture with a general degradation function and plasticity induced crack generation. *Mechanics of Materials* 2018; 116: 33–48.

19. Cheng J, Tu X, Ghosh S. Wavelet-enriched adaptive hierarchical FE model for coupled crystal plasticity-phase field modeling of crack propagation in polycrystalline microstructures. *Computer Methods in Applied Mechanics and Engineering* 2020; 361: 112757.

20. Ma R, Sun W. FFT-based solver for higher-order and multi-phase-field fracture models applied to strongly anisotropic brittle materials. *Computer Methods in Applied Mechanics and Engineering* 2020; 362: 112781.

21. Hutchinson J. Elastic-plastic behaviour of polycrystalline metals and composites. *Proceedings of the Royal Society of London. A. Mathematical and Physical Sciences* 1970; 319: 247–272.

22. Turner P, Tomé C, Woo C. Self-consistent modelling of nonlinear visco-elastic polycrystals: an approximate scheme. *Philosophical Magazine A* 1994; 70: 689–711.

23. Michel JC, Suquet P. A model-reduction approach to the micromechanical analysis of polycrystalline materials. *Computational Mechanics* 2016; 57: 483–508.

24. Hernández J, Oliver J, Huespe AE, Caicedo M, Cante J. High-performance model reduction techniques in computational multiscale homogenization. *Computer Methods in Applied Mechanics and Engineering* 2014; 276: 149–189.

25. Yu C, Kafka OL, Liu WK. Self-consistent clustering analysis for multiscale modeling at finite strains. *Computer Methods in Applied Mechanics and Engineering* 2019; 349: 339–359.

26. Liu Z, Kafka OL, Yu C, Liu WK. Data-driven self-consistent clustering analysis of heterogeneous materials with crystal plasticity. In: Springer. 2018 (pp. 221–242).

27. Kotha S, Ozturk D, Ghosh S. Parametrically homogenized constitutive models (PHCMs) from micromechanical crystal plasticity FE simulations, part I: Sensitivity analysis and parameter identification for Titanium alloys. *International Journal of Plasticity* 2019; 120: 296–319.

28. Nasri MA, Robert C, Ammar A, El Arem S, Morel F. Proper generalized decomposition (PGD) for the numerical simulation of polycrystalline aggregates under cyclic loading. *Comptes Rendus Mécanique* 2018; 346: 132–151.

29. Van Houtte P, Li S, Seefeldt M, Delannay L. Deformation texture prediction: from the Taylor model to the advanced Lamel model. *International Journal of Plasticity* 2005; 21: 589–624.

30. Tjahjanto D, Eisenlohr P, Roters F. A novel grain cluster-based homogenization scheme. *Modelling and Simulation in Materials Science and Engineering* 2009; 18: 015006.

31. Zhang X, Oskay C. Eigenstrain based reduced order homogenization for polycrystalline materials. *Computer Methods in Applied Mechanics and Engineering* 2015; 297: 408–436.

32. Zhang X, Oskay C. Sparse and scalable eigenstrain-based reduced order homogenization models for polycrystal plasticity. *Computer Methods in Applied Mechanics and Engineering* 2017; 326: 241–269.

33. Liu Y, Zhang X, Zhu Y, Hu P, Oskay C. Dislocation density informed eigenstrain based reduced order homogenization modeling: verification and application on a titanium alloy structure subjected to cyclic loading. *Modelling and Simulation in Materials Science and Engineering* 2020; 28: 025004.

34. Zhang X, Liu Y, Oskay C. Multiscale reduced-Order modeling of a Titanium skin panel subjected to thermomechanical loading. *AIAA Journal* 2022; 60: 302–315.

35. Xia D, Zhang X, Oskay C. Large-deformation reduced order homogenization of polycrystalline materials. *Computer Methods in Applied Mechanics and Engineering* 2021; 387: 114119.

36. Liu Z, Wu C, Koishi M. A deep material network for multiscale topology learning and accelerated nonlinear modeling of heterogeneous materials. *Computer Methods in Applied Mechanics and Engineering* 2019; 345: 1138–1168.

37. Liu Z, Wu C, Koishi M. Transfer learning of deep material network for seamless structure–property predictions. *Computational Mechanics* 2019; 64: 451–465.

38. Weber G, Pinz M, Ghosh S. Machine learning-aided parametrically homogenized crystal plasticity model (PHCPM) for single crystal Ni-based superalloys. *JOM* 2020; 72: 4404–4419.

39. Yuan M, Paradiso S, Meredig B, Niezgoda SR. Machine learning–based reduce order crystal plasticity modeling for ICME applications. *Integrating Materials and Manufacturing Innovation* 2018; 7: 214–230.

40. Dai W, Wang H, Guan Q, Li D, Peng Y, Tomé CN. Studying the micromechanical behaviors of a polycrystalline metal by artificial neural networks. *Acta Materialia* 2021; 214: 117006.

41. Huang D, Fuhg JN, Weißenfels C, Wriggers P. A machine learning based plasticity model using proper orthogonal decomposition. *Computer Methods in Applied Mechanics and Engineering* 2020; 365: 113008.

42. Oskay C, Fish J. Eigendeformation-based reduced order homogenization for failure analysis of heterogeneous materials. *Computer Methods in Applied Mechanics and Engineering* 2007; 196: 1216–1243.

43. Brandyberry DR, Zhang X, Geubelle PH. A GFEM-based reduced-order homogenization model for heterogeneous materials under volumetric and interfacial damage. *Computer Methods in Applied Mechanics and Engineering* 2021; 377: 113690.

44. Liu Z. Deep material network with cohesive layers: Multi-stage training and interfacial failure analysis. *Computer Methods in Applied Mechanics and Engineering* 2020; 363: 112913.

45. Oliver J, Linero DL, Huespe AE, Manzoli OL. Two-dimensional modeling of material failure in reinforced concrete by means of a continuum strong discontinuity approach. *Computer Methods in Applied Mechanics and Engineering* 2008; 197: 332–348.

46. Robinson J, Beevers C. The effects of load ratio, interstitial content, and grain size on low-stress fatigue-crack propagation in α-titanium. *Metal Science Journal* 1973; 7(1): 153–159.

47. Irving P, Beevers C. The effect of air and vacuum environments on fatigue crack growth rates in Ti-6Al-4V. *Metallurgical and Materials Transactions B* 1974; 5: 391–398.

48. Ward-Close C, Beevers C. The influence of grain orientation on the mode and rate of fatigue crack growth in α-titanium. *Metallurgical Transactions A* 1980; 11: 1007–1017.

49. Gao Y, Stölken J, Kumar M, Ritchie R. High-cycle fatigue of nickel-base superalloy René 104 (ME3): Interaction of microstructurally small cracks with grain boundaries of known character. *Acta Materialia* 2007; 55: 3155–3167.

50. Schaef W, Marx M, Vehoff H, Heckl A, Randelzhofer P. A 3-D view on the mechanisms of short fatigue cracks interacting with grain boundaries. *Acta Materialia* 2011; 59: 1849–1861.

51. Zhang K, Wu X, Davies C. Effect of microtexture on short crack propagation in two-phase titanium alloys. *International Journal of Fatigue* 2017; 104: 206–220.

52. Terada K, Hori M, Kyoya T, Kikuchi N. Simulation of the multi-scale convergence in computational homogenization approaches. *International Journal of Solids and Structures* 2000; 37: 2285–2311.

53. Guedes J, Kikuchi N. Preprocessing and postprocessing for materials based on the homogenization method with adaptive finite element methods. *Computer Methods in Applied Mechanics and Engineering* 1990; 83: 143–198.

54. Zhang S, Oskay C. Reduced order variational multiscale enrichment method for elasto-viscoplastic problems. *Computer Methods in Applied Mechanics and Engineering* 2016; 300: 199–224.

55. Marfia S, Sacco E. Computational homogenization of composites experiencing plasticity, cracking and debonding phenomena. *Computer Methods in Applied Mechanics and Engineering* 2016; 304: 319–341.

56. Hu R, Oskay C. Nonlocal homogenization model for wave dispersion and attenuation in elastic and viscoelastic periodic layered media. *Journal of Applied Mechanics* 2017; 84: 031003.

57. Bogdanor MJ, Oskay C. Prediction of progressive fatigue damage and failure behavior of IM7/977-3 composites using the reduced-order multiple space-time homogenization approach. *Journal of Composite Materials* 2017; 51: 2101–2117.

58. Moyeda A, Fish J. Multiscale analysis of solid, waffle, ribbed and hollowcore reinforced concrete slabs. *Computer Methods in Applied Mechanics and Engineering* 2019; 348: 139–156.

59. Sparks P, Oskay C. Identification of optimal reduced order homogenization models for failure of heterogeneous materials. *International Journal for Multiscale Computational Engineering* 2013; 11.

60. Liu Z, Bessa M, Liu WK. Self-consistent clustering analysis: an efficient multi-scale scheme for inelastic heterogeneous materials. *Computer Methods in Applied Mechanics and Engineering* 2016; 306: 319–341.

61. Alaimo G, Auricchio F, Marfia S, Sacco E. Optimization clustering technique for pieceWise uniform transformation field analysis homogenization of viscoplastic composites. *Computational Mechanics* 2019; 64: 1495–1516.

62. Quey R, Kasemer M. The Neper/FEPX project: free/open-source polycrystal generation, deformation simulation, and post-processing. In: . 1249. IOP Publishing. ; 2022: 012021.

63. Geuzaine C, Remacle JF. Gmsh: A 3-D finite element mesh generator with built-in pre-and post-processing facilities. *International Journal for Numerical Methods in Engineering* 2009; 79: 1309–1331.

64. Chaboche JL, Kruch S, Maire JF, Pottier T. Towards a micromechanics based inelastic and damage modeling of composites. *International Journal of Plasticity* 2001; 17: 411–439.

65. Fish J, Filonova V, Yuan Z. Hybrid impotent–incompatible eigenstrain based homogenization. *International Journal for Numerical Methods in Engineering* 2013; 95: 1–32.

66. Proudhon H, Li J, Ludwig W, Roos A, Forest S. Simulation of short fatigue crack propagation in a 3D experimental microstructure. *Advanced Engineering Materials* 2017; 19: 1600721.

□

APPENDIX

A EXPRESSION OF THE COEFFICIENT TENSORS AND INDIVIDUAL TERMS IN EQS. (10) AND (11)

$$M^{(\alpha)}_{ijkl} = \int_{\Theta} \psi^{(\alpha)}_{\text{ph}}(\mathbf{y}) M_{ijkl}(\mathbf{y}) N^{(\alpha)}_{\text{ph}}(\mathbf{y}) d\mathbf{y} \tag{A1}$$

$$P^{(\alpha\beta)}_{ijkl} = \int_{\Theta}\int_{\Theta} \psi^{(\alpha)}_{\text{ph}}(\mathbf{y}) N^{(\beta)}_{\text{ph}}(\hat{\mathbf{y}}) g^{\text{ph}}_{ijkl}(\mathbf{y},\hat{\mathbf{y}}) d\hat{\mathbf{y}} d\mathbf{y} \tag{A2}$$

$$A^{(\alpha)}_{ijkl} = \int_{\Theta} \psi^{(\alpha)}_{\text{ph}}(\mathbf{y}) A_{ijkl}(\mathbf{y}) d\mathbf{y} \tag{A3}$$

$$R^{(\alpha\gamma)}_{ijm} = \int_{\Theta} \psi^{(\alpha)}_{\text{ph}}(\mathbf{y}) \int_{S} g^{\text{sep}}_{ijm}(\mathbf{y},\hat{\mathbf{y}}) N^{(\gamma)}_{\text{sep}}(\hat{\mathbf{y}}) d\hat{\mathbf{y}} d\mathbf{y} \tag{A4}$$

in which $\mathbf{M}$ is the inverse of the elasticity tensor $\mathbf{L}$.

$$t^{(\gamma)}_{p}(t) = \int_{S} \psi^{(\gamma)}_{\text{sep}}(\hat{\mathbf{y}}) t_{p}(\hat{\mathbf{y}}, t) d\hat{\mathbf{y}} \tag{A5}$$

$$C^{(\gamma)}_{pmn} = \int_{S} \psi^{(\gamma)}_{\text{sep}}(\hat{\mathbf{y}}) \int_{\Theta} g^{\text{sep}}_{ijp}(\mathbf{y},\hat{\mathbf{y}}) L_{ijkl}(\mathbf{y}) A_{klmn}(\mathbf{y}) d\mathbf{y} d\hat{\mathbf{y}} \tag{A6}$$

$$D^{(\gamma\eta)}_{pm} = \int_{S} \psi^{(\gamma)}_{\text{sep}}(\hat{\mathbf{y}}) D^{(\eta)}_{pm}(\hat{\mathbf{y}}) d\hat{\mathbf{y}} \tag{A7}$$

$$T^{(\gamma\alpha)}_{pmn} = \int_S \psi^{(\gamma)}_{\text{sep}}(\hat{\mathbf{y}}) T^{(\alpha)}_{pmn}(\hat{\mathbf{y}}) d\hat{\mathbf{y}} \tag{A8}$$

in which,

$$D^{(\eta)}_{pm}(\hat{\mathbf{y}}) = \int_\Theta g^{\text{sep}}_{ijp}(\mathbf{y}, \hat{\mathbf{y}}) L_{ijkl}(\mathbf{y}) R^{(\eta)}_{klm}(\mathbf{y}) d\mathbf{y} \tag{A9}$$

$$R^{(\eta)}_{klm}(\mathbf{y}) = \int_S N^{(\eta)}_{\text{sep}}(\hat{\mathbf{y}}) g^{\text{sep}}_{klm}(\mathbf{y}, \hat{\mathbf{y}}) d\hat{\mathbf{y}} \tag{A10}$$

$$T^{(\alpha)}_{pmn}(\hat{\mathbf{y}}) = \int_\Theta g^{\text{sep}}_{ijp}(\mathbf{y}, \hat{\mathbf{y}}) L_{ijkl}(\mathbf{y}) S^{(\alpha)}_{klmn}(\mathbf{y}) d\mathbf{y} \tag{A11}$$

$$S^{(\alpha)}_{klmn}(\mathbf{y}) = \int_\Theta N^{(\alpha)}_{\text{ph}}(\hat{\mathbf{y}}) \left[g^{\text{ph}}_{klmn}(\mathbf{y}, \hat{\mathbf{y}}) - I_{klmn} \delta(\mathbf{y} - \hat{\mathbf{y}}) \right] d\hat{\mathbf{y}} \tag{A12}$$

B BRIEF INTRODUCTION OF REVERSIBLE DISLOCATION-DENSITY BASED CRYSTAL PLASTICITY

The proposed reduced order framework is not restricted to any specific slip evolution model[31]. In the current work, we adopt a reversible dislocation-density based crystal plasticity model proposed in[33]. The equations are summarized as follows:

- Flow rule:

$$\dot{\gamma}^s = \frac{\rho^s_m v^s_{id} (b^s)^2}{2} \text{sgn}(\tau^s) \exp\left(\frac{-\Delta F^s}{k\theta}\right) \exp\left(\frac{(\tau^s - s^s)\Delta V^s}{k\theta}\right) \tag{B13}$$

- Schmid law:

$$\tau^s = \sigma_{ij} Z^s_{ij} \tag{B14}$$

- Hardening evolution

$$s^s(\dot{\gamma}^s) = s^s_0 + s^s_{for}(\dot{\gamma}^s) + s^s_{deb}(\dot{\gamma}^s) \tag{B15}$$

$$s^s_{for}(\dot{\gamma}^s) = \mu \chi b^s \sqrt{\rho^s_{for}} \tag{B16}$$

$$s^s_{deb}(\dot{\gamma}^s) = \mu b^s k_{deb} \sqrt{\rho_{deb}} \ln\left(\frac{1}{b^s \sqrt{\rho_{deb}}}\right) \tag{B17}$$

- Dislocation density evolution

1. forest dislocation density

$$\rho^s_{for} = \rho^s_{fwd} + \rho^{s+}_{rev} + \rho^{s-}_{rev} \tag{B18}$$

$$\frac{\partial \rho^s_{fwd}}{\partial \gamma^s} = (1-p) k^s_1 \sqrt{\rho^s_{for}} - k^s_2(\dot{\gamma}^s, \theta) \rho^s_{for} \tag{B19}$$

$$k^s_2(\dot{\gamma}^s, \theta) = k^s_1 \frac{b^s \chi}{g^s} \left[1 - \frac{k\theta}{\hat{D} b^{s^3}} \ln\left(\frac{\dot{\gamma}^s}{\dot{\gamma}_0}\right)\right] \tag{B20}$$

– if $\tau^s > 0$:

$$\frac{\partial \rho^{s+}_{rev}}{\partial \gamma^s} = p k^s_1 \sqrt{\rho^s_{for}} - k^s_2(\dot{\gamma}^s, \theta) \rho^{s+}_{rev} \tag{B21}$$

$$\frac{\partial \rho^{s-}_{rev}}{\partial \gamma^s} = -k^s_1 \sqrt{\rho^s_{for}} \left(\frac{\rho^{s-}_{rev}}{\rho^s_0}\right)^{\hat{m}} \tag{B22}$$

– if $\tau^s < 0$:

$$\frac{\partial \rho^{s-}_{rev}}{\partial \gamma^s} = p k^s_1 \sqrt{\rho^s_{for}} - k^s_2(\dot{\gamma}^s, \theta) \rho^{s-}_{rev} \tag{B23}$$

$$\frac{\partial \rho^{s+}_{rev}}{\partial \gamma^s} = -k^s_1 \sqrt{\rho^s_{for}} \left(\frac{\rho^{s+}_{rev}}{\rho^s_0}\right)^{\hat{m}} \tag{B24}$$

Table B1 Model parameters for the dislocation density based crystal plasticity model

Symbols	**Units**	**Basal** $< a >$	**Prismatic** $< a >$	**Pyramidal** $< a >$	**Pyramidal** $< c + a >$
ΔF^s	J	3.95×10^{-20}	3.81×10^{-20}	4.27×10^{-20}	4.73×10^{-20}
ΔV^s	m^3	5.91×10^{-29}	8.20×10^{-29}	7.40×10^{-29}	8.85×10^{-29}
k	$J \cdot K^{-1}$	1.38×10^{-23}	1.38×10^{-23}	1.38×10^{-23}	1.38×10^{-23}
ρ_m^s	m^{-2}	5.00×10^{12}	5.00×10^{12}	5.00×10^{12}	5.00×10^{12}
v_{id}^s	Hz	1.00×10^{12}	1.00×10^{12}	1.00×10^{12}	1.00×10^{12}
b^s	μm	2.94×10^{-4}	2.95×10^{-4}	2.95×10^{-4}	4.68×10^{-4}
s_0^s	MPa	500	435	680	677
k_1^s	m^{-1}	1.80×10^7	1.68×10^7	1.67×10^7	2.4×10^7
D^s	MPa	300	330	100	90

2. debris dislocation density

$$d\rho_{deb} = \sum_s \frac{\partial \rho_{deb}^s}{\partial \gamma^s} d\gamma^s \tag{B25}$$

$$\frac{\partial \rho_{deb}^s}{\partial \gamma^s} = q b^s \sqrt{\rho_{deb}} k_2^s(\dot{\gamma}^s, \theta) \rho_{for}^s \tag{B26}$$

The model parameters are shown in Table B1 [33,34].